UNIVERSITY OF CALIFORNIA SAN DIEGO

Use of Hyperspectral Imaging for the Study of Hemoglobin Oxygen Saturation in the Microcirculation

A thesis submitted in partial satisfaction of the
requirements for the degree
Master of Science

in

Bioengineering

by

Alfredo Lucas

Committee in charge:

Professor Pedro Cabrales, Chair
Professor Marcos Intaglietta
Professor Kevin King
Professor Tatum Simonson

2019

The thesis of Alfredo Lucas is approved, and it is acceptable in quality and form for publication on microfilm and electronically:

_____

_____

_____

_____

Chair

University of California San Diego

2019

TABLE OF CONTENTS

LIST OF FIGURES

LIST OF TABLES

ACKNOWLEDGEMENTS

I would like to thank Dr. Pedro Cabrales for the immense support not only while pursuing my Masters degree under his supervision, but also throughout my undergraduate career at UC San Diego. His support was instrumental throughout my time at this institution. I would also like to thank my labmates and friends Carlos Munoz, Alexander Williams, Cynthia Walser, Vivek Jani, Cynthia Muller, Krianthan Govender, and Amanda Breton for their technical and emotional support at many stages throughout this process. I would like to specifically thank Carlos Munoz for his tremendous help during the animal experiments presented in this document, and Cynthia Walser for all the surgical preparations, without which this would have been, quite literally, impossible.

I would also like to thank my family. My father, for his unconditional support and superhuman effort in helping me and my sister stay afloat in this country. Without his efforts and teachings, I would not be who I am today. Ana, for unconditionally loving and supporting my father and me. My sister, for being a source of energy and happiness, regardless of adversity. My mother, for her love and for always being a source of advice. Vasiliki, for her love and for always being there for me.

This thesis, in full, is currently being prepared for submission for publication of the material. Lucas, Alfredo; Munoz, Carlos; Cabrales, Pedro. The thesis author was the primary author of this material.

ABSTRACT OF THE THESIS

Use of Hyperspectral Imaging for the Study of Hemoglobin Oxygen Saturation in the Microcirculation

by

Alfredo Lucas
Master of Science in Bioengineering

University of California San Diego 2019

Professor Pedro Cabrales, Chair

Hyperspectral imaging is an imaging modality that combines imaging and spectroscopy in the same system. The ability to combine spectral and spatial information in the same modality allows for spectral analysis at every spatial location in a given image. This thesis will present a novel hyperspectral imaging approach for the study of the microcirculation *in vivo*. The approach involves the use of a spatial-scanning hyperspectral imaging technique, coupled with an efficient processing pipeline. Much of the literature involving the use of hyperspectral imaging for the study of the microcirculation *in vivo* has focused in very spatially limited approaches that involve the use of spectral-scanning hyperspectral imaging systems. With the

spatial-scanning approach, a wider field of view, and superior spatial resolution is achieved, allowing for better averaging and higher statistical power in the results. Chapter 1 is a brief introduction. Chapter 2 presents a literature review of the different hyperspectral imaging modalities and their respective biomedical applications. A comprehensive review of the current state of the literature regarding the use of hyperspectral imaging for the study of the microcirculation *in vivo* is also included. Chapter 3 presents a work currently submitted for publication in which a spatial-scanning hyperspectral imaging approach is used to study hypoxia dynamics in a hamster window chamber model. Chapter 4 presents a mathematical modeling of post-hypoxic hemoglobin reoxygenation dynamics in a mouse window chamber, measured by hyperspectral imaging. Finally, Chapter 5 presents the use of hyperspectral imaging for the monitoring of hemoglobin oxygenation dynamics during hemorrhagic shock onset, resuscitation and recovery.

Chapter 1

Introduction

The microcirculation is the primary oxygen exchange center of the circulatory system. The study of oxygen transport and delivery in the microcirculation has been a key subject of interest for physiologists, clinicians and engineers alike. A wide variety of techniques, experimental designs and models have been developed just for the study of this particular subject, but to this day, there still is a lot to be understood.

Hyperspectral imaging is an imaging modality that combines imaging and spectroscopy in the same system. The ability to combine spectral and spatial information in the same modality allows for spectral analysis at every spatial location in a corresponding image. This is of particular use in the study of the microcirculation, where blood vessels and their interactions with the surrounding tissue are the primary subjects of study. Hemoglobin, the oxygen carrying molecule present in blood, has very different spectral properties when it is bound to oxygen, relative to when it is unbound. Using the characteristic spectral signatures of hemoglobin, techniques like hyperspectral imaging can provide spatially-varying oxygen saturation maps in imaged regions of the microcirculation. The ability to observe the varying spatial gradients in hemoglobin oxygenation, as well as how those gradients change over time

and under different environmental conditions, such as hypoxia, can provide valuable insight about oxygen transport and exchange in the microcirculation.

This thesis will present a novel hyperspectral imaging approach for the study of the microcirculation *in vivo*. The approach involves the use of a spatial-scanning hyperspectral imaging technique, coupled with an efficient processing pipeline. Much of the literature involving the use of hyperspectral imaging for the study of the microcirculation *in vivo* has focused in very spatially limited approaches that involve the use of spectral-scanning hyperspectral imaging systems. With the spatial-scanning approach, a wider field of view, and superior spatial resolution is achieved, allowing for better averaging and higher statistical power in the results. The structure of the thesis is as follows: Chapter 2 presents a literature review of hyperspectral imaging it modalities with their corresponding biomedical applications. It also presents a comprehensive review of the current state of the literature regarding the use of hyperspectral imaging for the study of the microcirculation *in vivo*, in particular in animal window chamber models. Chapter 3 presents a work currently submitted for publication in which a spatial-scanning hyperspectral imaging approach is used to study hypoxia dynamics in a hamster window chamber model. Chapter 4 presents the mathematical modeling of post-hypoxic hemoglobin reoxygenation dynamics in a mouse window chamber, as measured by the hyperspectral imaging approach proposed in Chapter 3. Finally Chapter 5 presents a preliminary use-case scenario of the methodology from Chapter 3, where hyperspectral imaging is used for the monitoring of hmeoglobin oxygenation dynamics during hemorrhagic shock onset, resuscitation and recovery.

Chapter 2

Literature Review

This chapter will present an overview of the uses of hyperspectral imaging for biomedical applications. A brief mention to all the hyperspectral imaging modalities as well as their biomedical applications will be presented. Towards the end of the chapter, particular emphasis will be placed in the applications of hyperspectral imaging for the study of the microcirculation. Throughout this and the following chapters the term HSI will be used to refer to hyperspectral imaging (the modality), and to refer to the hyperspectral image itself (the output of the modality).

2.1 Hyperspectral Imaging and its Modalities

Hyperspectral imaging (HSI) is the combination of imaging and spectroscopy in a single modality. The origins of HSI, also known as imaging spectrometry, can be dated back to the late 70s and early 80s when NASA used a primitive form of the technology for remote sensing applications [1]. Early applications were primarily focused in the study of vegetation and terrains. Since early satellite-based implementations, HSI has evolved significantly, and has been used for a wide variety of applications including art conservation [2], food quality control [3], and forensics [4].

Furthermore, recent improvements in computational processing capabilities, have allowed hyperspectral imaging to become increasingly more accessible to consumers. The increase in accessibility to hyperspectral imagers has not only allowed for an exponential increase in the uses of HSI [5], but also has allowed biomedical researchers to exploit the technology in their favor, resulting in more than 28 different applications of HSI in medicine [6], with many more applications in molecular biology and microscopy [7]. The presence of spectrally active compounds such as hemoglobin (Hb) and melanin make HSI an ideal tool for clinically relevant biomedical applications, particularly in the fields of dermatology [8] and ophtalmology [9]. The rest of this section will focus on the basic components and biomedical uses of HSI, whereas the next section will focus on the uses HSI for the study of oxygen dynamics in the microcirculation.

2.1.1 The Hypercube

HSI allows for the simultaneous acquisition of spectral and spatial information. Given this, each hyperspectral image can be thought of as a 3-dimensional dataset consisting of 2 spatial dimensions and a 3rd spectral dimension. This hyperspectral data structure is often referred to as a hypercube (Figure 2.1). In the hypercube, the X and Y dimensions are often referred to as the spatial dimensions, while the Z dimension is the spectral dimension. Each (X, Y) set of coordinates, for a fixed Z, is often referred to as a spectral band (shown as one of the different colored images in Figure 2.1). Each spectral band then consists of spatial variations in intensity measured at a specific wavelength. These variations in intensity represent variations in reflectance, or absorbance, depending on the experimental and system setup.

This hypercube representation allows for convenient comparisons with more traditional imaging modalities. For example, a greyscale image can be defined as a

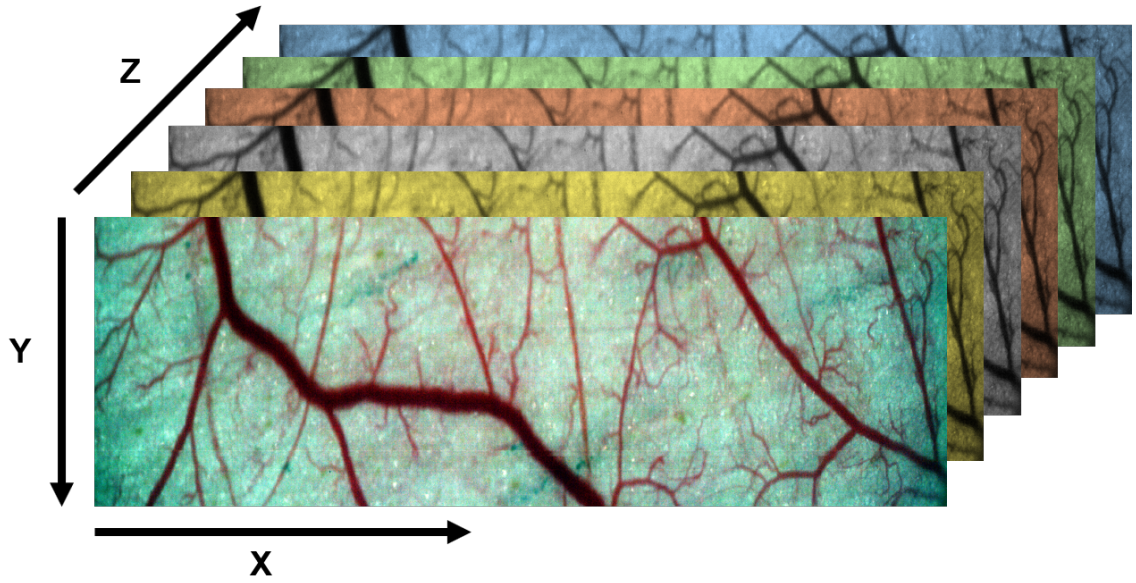

Figure 2.1: Graphical representation of a hyperspectral hypercube. The X and Y dimensions are the spatial dimensions, while the Z dimension is the spectral dimension. The orientation of the axes was chosen to be consistent with the digital representation of the hypercube.

single slice of the hypercube, whereas a traditional color image (RGB image) can be thought of the image resulting by combining the intensities of the spectral bands corresponding to the red, green and blue wavelengths. In reality, this analogy is not entirely accurate since more in-depth colorimetric conversions are required to fully generate a true RGB conversion from a spectral representation [10]. However, for a first exposure to HSI, this interpretation helps to understand the principles behind HSI. Another imaging modality, which is often times assumed to be the same as hyperspectral imaging, is multispectral imaging (MSI). Much like HSI, MSI acquires both spatial and spectral information and uses a hypercube as its main data structure. The key difference between both modalities is their spectral resolution. HSI often collects information from contiguous spectral bands often separated by 2nm,

5nm or 10nm, whereas MSI often collects information from non-contiguous spectral bands, often separated by more than 50nm, but different criteria is used to classify them [11]. Clearly, the decreased spectral resolution of MSI allows for decreased acquisition times, since less information is acquired per image, but this comes at the expense of decreased ability to resolve certain important spectral features. Care will be taken during the remainder of this review to distinguish between the two.

2.1.2 General Hardware

A HSI hypercube contains both spectral and spatial information, therefore, the hardware must involve a combination of spectrometry and optical imaging components. In general, a HSI system will contain: a dispersive element, a set of optical elements (i.e. lenses, objectives, mirrors, etc.), an illumination source and a detector array.

Dispersive Elements

The dispersive elements are in charge of decomposing the incoming light into its corresponding spectral constituents. There are multiple types of dispersive elements commonly used in medical HSI applications: monochromators, optical bandpass filters and single-shot imagers, and as noted later, these will also be the key distinctions between the different HSI modalities.

The monochromator based spectral elements involve either a prism or a grating element that allow incoming polychromatic light to be decomposed into its constitutive spectra. A prism monochromator works under the principle that light of different wavelengths will get bent at different angles upon exciting the prism, generating the constitutive spectra [12]. A grating monochromator uses a collimation-type grid with different spacings between adjacent portions of the grid. If the spacing between adjacent grid columns is smaller than a given wavelength, only light under

that wavelength will pass through the element. In principle, both types of dispersive elements are capable of decomposing the incoming light into its constitutive spectra, however, they are suitable for different applications. While allowing for high-throughput transmission and minimal scattering above the UV and below the IR range, prisms possess a non-linear wavelength dispersion, and limits applications to the visible range. Furthermore, proper applications involve compound prism design or complex detection optics in order to obtain the resultant spectra [13]. Grating elements, on the other hand, are less expensive than prisms, and allow for much simpler and compact designs, but suffer from scattering and lower throughput [14]. A third alternative to prism and grating elements is to use a prism-grating-prism element (PGP) which combines the benefits of prism and grating elements in a cost-efficient solution [15]. Due to the way monochromator dispersive elements work, they are only capable of acquiring a single point or line of the imaged sample at a time.

Optical bandpass filters are the second way in which HSI systems can decompose the incoming light into its constitutive spectra. As the name suggests, they involve the use of a series of bandpass filters which are alternated in order to acquire images at different bandpass ranges. An evident limitation of this approach, when compared to monochromator based HSI systems, is that they have a much smaller spectral resolution, therefore they are mostly used in MSI systems. Common approaches involving optical bandpass filters consist in using a filter wheel that can be automatically rotated in order to acquire images at different wavelengths [16]. This approach while convenient, it falls under the MSI domain.

As an alternative to mechanical control of the bandpass filters, electrically controlled tunable filters are often used, allowing for faster acquisition and spectral resolutions that fall under the hyperspectral domain. Currently, there are two main types of tunable filters, liquid crystal tunable filters (LCTF) and acousto-optical tunable filters (AOTF) [17, 18]. LCTF often consist of a series of birefirngent quartz crystals which deform upon the application of a voltage. The deformation of the

crystals leads to changes in the index of refraction of the system, which results in a selective retardation of specific wavelengths of the incident light [17]. The exiting light then goes through a polarizer that allows light with only a specific phase retardation to go through, successfuly acting as a bandpass filter. Changes in the applied voltage will allow for light of different wavelengths to go through, effectively matching the applied voltage to the bandpass range of the filter. AOTF also involves the use of birefringent crystals, but instead of using a fixed voltage to change the curvature of the crystal, radio-frequency waves, modulated by a piezoelectric, are sent through the crystal medium. The acoustic waves generated inside the crystal changes its index of refraction and effectively changes the phase retardation of the incoming light at different wavelengths [19]. Optical bandpass filters capture one wavelength at a time, as compared to monochromators, where every single wavelength is captured for the imaged line or point. Furthermore, optical bandpass filters allow for fine tuned wavelength selection, allowing the HSI system to only acquire the required wavelengths, expediting the image acquisition process.

A final type of type of dispersive element involves the use of a computer-generated hologram, where spatial and spectral information are acquired simultaneously with a single acquisition. In this approach, a two-dimensional grating disperser is used. The grating element generates multiple projections of the imaged region that can be digitally reconstructed into a HSI [9]. A clear advantage of this approach is the increased temporal resolution when compared with the other dispersive elements, but it suffers from lack of both spatial and spectral resolution. In fact, many of the applications involving the use of this approach actually fall under the MSI domain given the limited spectral resolution [11].

Detector Array

The detector arrays used in HSI applications often involve a 2-dimensional array designed to measure the light intensity that exits the dispersive element. The use

of a 2-dimensional array significantly decreases acquisition time and computational reconstruction, and is by far the most commonly used array geometry in HSI applications, although 1-dimensional line arrays can also be used for point-scanning systems [20]. Among the different types of detectors that can be used for HSI applications we find: charged coupled devices (CCD), intensified and electron multiplying CCDs (ICCD and EMCCD), photomultiplier tubes (PMT) and complementary metal oxide semiconductors (CMOS). PMT, ICCD and EMCCD are often used for low-light, high temporal resolution applications since they require little light exposure in order to generate the image, whereas CMOS and CCD devices require longer exposure times in order to produce a high quality image. Furthermore, between CMOS and CCDs, the latter are preferred since CMOS often have a much higher dark current and noise than CCDs [6].

2.1.3 HSI Modalities

HSI has different modalities, all of which are distinguished by the way in which the hypercube is generated, that is, they are distinguished by the type of dispersive element used and how the dispersive element projects the acquired information into the detector array. The three main types of HSI modalities are: spectral scanning, spatial scanning and snapshot HSI. A summary of each modality and some clinical uses are shown in Table 2.1.

Spectral Scanning HSI

Spectral scanning HSI systems (also referred to as staring HSI systems), as the name suggests, generate the hypercube one spectral band at the time. Therefore, during acquisition, the X and Y dimensions of the hypercube are projected simultaneously onto the detector array, whereas each spectral band in the Z direction is obtained with subsequent acquisitions. Therefore, the hypercube is built by

stacking subsequent acquisitions in the (X, Y) plane at fixed Z values. This imaging approach is achieved through the use of an optical bandpass filter dispersive element, often consisting of a LTCF or a AOTF, as previously mentioned. Spectral scanning systems take advantage of the fast transition times between selectable wavelengths that LTCF and AOTF provide, allowing for relatively fast image acquisition. Furthermore, AOTF can provide spectral resolutions of as low as $3nm$ [17]. Spatially, however, they are limited by the field-of-view of the coupled optics, and by the spatial resolution of the coupled filter (AOTF will have a lower spatial resolution than a LTCF due to opto-acoustic effects) [6, 18, 17]. Biomedical applications for spectral scanning HSI systems have involved the study of: burn wounds [21], breast [22] and prostate cancer [23], diabetic wounds [24], tumor hypoxia [25], skin cancer [26], hemorrhagic shock [27] and laparoscopic surgery [28]. Note that some of these application such as the tumor hypoxia, laparoscopic surgery and hemorrhagic shock monitoring require high temporal resolution.

Spatial Scanning HSI

Spatial scanning HSI systems scan the imaged region spatially while acquiring all the spectral information during each acquisition. The two main types of spatial scanning HSI systems are: the point-scan (wiskbroom) and the line-scan (pushbroom) HSI systems. As the name suggests, in the point-scan HSI system, the hypercube is constructed by acquiring a single spatial location at a time. Using Figure 2.1 as a reference, in the point-scan HSI system, all the spectral components in the Z direction for a fixed (X, Y) spatial location are acquired at any given time. Subsequent acquisitions then translate the imager or the imaging region in the (X, Y) plane, acquiring the spectral information from the entirety of the sample. While having high spatial and spectral resolution, this approach suffers from very low temporal resolution and therefore its applications are limited confocal-scanning coupled approaches [29]. For the line-scanning HSI system, all elements in the Z

direction for a given vertical line in the Y direction, at a fixed X, are acquired. Subsequent acquisitions physically translate the imaging region in the X direction in order for subsequent lines to be acquired. Therefore, the hypercube is built by stacking subsequent acquisitions in the (Y, Z) plane at fixed X values. Based on the way they operate, line-scanning HSI systems use monochromator based dispersive elements coupled with a 2-dimensional detector array. This allows for high spatial and spectral resolution at the expense of low temporal resolution, resulting from the mechanical translation of the imaging region or of the imager itself. Biomedical applications of spatial-scanning HSI systems have involved the study of: cutaneous wounds [30], melanoma [31], intestinal ischemia [32] and gastric cancer [33], as well as microarray DNA [34, 35] and quantum dot visualization [36]. Careful observation of these applications shows that they do not require high temporal resolutions and they can be implemented either in a large space or allow for translation of the imaging stage, being ideal applications for the lower temporal resolution and required translation of the sample characteristic of spatial-scanning HSI systems.

Snapshot HSI

Snapshot HSI systems acquire both spectral and spatial information in a single image, hence the name snapshot. Snapshot HSI systems are based on the use of 2-dimensional dispersion grating elements, or highly specialized prisms, that project multiple views of the field-of-view into different quadrants of the detector array. Each projection then contains spectral information from a single wavelength. This is equivalent to having a 2-dimensional hypercube, where both the X and Y direction are elongated by concatenating spectral bands from the Z dimension. Since both spectral and spatial information are acquired simultaneously, a single acquisition is required to generate the hypercube, which can subsequently be reshaped to exhibit the canonical form shown in Figure 2.1. However, given that both spatial and spectral information now have to be compressed into the same detector array, there has to be

a significant tradeoff in spatial and/or spectral resolution. This modality has been used in highly specialized systems for ophtalmologic [9] and endoscopic applications [37].

Table 2.1: Comparison of HSI modalities with corresponding biomedical applications. **Wavelength Selectability** corresponds to the ability, of the specific modality, to chose the acquisition of specific spectral bands. Partially adapted from Lu et. al. [6] and Li et. al. [11]

	Spectral Scanning	**Spatial Scanning**	**Snapshot**
Dispersive Element	Filter wheels, AOTF, LCTF, digital grating switching monochromators	Prism, grating and PGP	2-dimensional dispersion grating, combination of beamsplitters and filters
Wavelength Selectability	Readily available	Limited	Limited
Hypercube Acquisition Time (temporal resolution)	Short	Long	Very Short
Spatial Resolution	Low	High	Very Low
Spectral Resolution	Medium	High	Low
Medical Applications	Burn wounds [21], breast [22] and prostate cancer [23], diabetic wounds [24], tumor hypoxia [25], skin cancer [26], hemorrhagic shock [27] and laparoscopic surgery [28]	Cutaneous wounds [30], melanoma [31], intestinal ischemia [32] and gastric cancer [33]	Retinal oxygenation [9, 38] and endoscopy [37]

2.2 Hyperspectral Imaging and the Study of Oxygen Transport in the Microcirculation

The circulatory system is in charge of the transport of nutrients and oxygen accross the body. The oxygen transport in the circulatory system takes place at the microcirculatory level in the domain of arterioles, venules and capillaries. Oxygen transport in the microcirculation has been extensively studied using both isolated cellular cultures and *in vivo* approaches. The use of cell cultures for the study of oxygen consumption has elucidated many important metabolic pathways [39, 40], but they are limited by the idealized environment of a cell culture, where often times, a partial pressure of oxygen (PO_2) dependence in oxygen consumption has been observed [41, 42]. For this reason, the use of *in vivo* models are preferred in an attempt to emulate the microcirculatory physiological environment as much as possible. This section will review the commonly used methods for *in vivo* microvascular oxygen measurements and compare them to HSI. A review of the literature on the use of HSI for the study of the microcirculation in intravital microscopy studies is presented at the end of this section.

2.2.1 Traditional Approaches for *In Vivo* Microvascular Oxygen Measurements

The development of instruments and techniques for the measurement of intravascular O_2 has a longstanding tradition. Some of the most widely used methods include: O_2 microelectrodes, phosphoresence quenching microscopy (PQM) and microspectrophotometry. A more detailed description of each of these approaches can be found in [41, 43], but their comparison to HSI will be mentioned briefly.

O_2 Microelectrodes

The use of O_2 microelectrodes is widespread in the literature. These Clark-type electrodes consist of a polarized catalytic surface, which allows for O_2 reduction upon contact. The electrode is then calibrated with substances of different PO_2, all within the dynamic range of measurements that will be carried out in the system. While the original designs for O_2 microelectrodes had significant oxygen consumption, improved designs such as the Whalen-type electrode, have significantly less oxygen consumption [44, 45]. While O_2 microelectrodes have been the preferred method for measuring O_2 in highly controlled environments such as cell cultures [46, 47], they have also been adapted for use *in vivo* [48]. Many of the measurements, however, are of perivascular PO_2, since vessel penetration often lead to vessel wall damage and platelet aggregation. This alone, significantly limits the applications of O_2 microelectrodes to the measurement of perivascular PO_2. In addition, the measurements are highly sensitive to the perivascular environment and require the constant use of perfusates such as phosphate-buffered saline to maintain proper pH and temperature [44]. These are all disadvantages of the use of O_2 microelectrodes when compared to HSI, which does not require any special conditions, other than exposure of the imaging area. Furthermore, HSI is a high-throughput approach, as it allows to measure Hb O_2 saturation (HbO_2) across the entirety of the imaged region, whereas microelectrode measurements are single-point measurements. An advantage of O_2 microelectrodes over HSI, however, is that they measure PO_2 directly, whereas HSI approaches rely on conversions from HbO_2 to PO_2 through the Hb disosciation curve, which can vary in the presence of different pathological conditions. HSI is also unable to measure PO_2 in the absence of Hb (e.g. the perivascular tissue).

Phosphorescence Quenching Microscopy

The use of phosphorescence quenching microscopy (PQM) for the measurement of PO_2 was developed in the late 80s by [42] and was originally applied to O_2 saturated aqueous solutions. Filho and Intaglietta [49] were the first to apply the technique in the microcirculation, specifically in a dorsal window chamber model of a hamster. Intaglietta, Tsai and Cabrales subsequently adopted a widespread use of the technique for a plethora of conditions [50, 51, 52], and is currently still used by our research group. The technique consists in using phosphor that can be excited by a pulse of light at a specific wavelength. After excitation, the phosphor decays over time to resting state and in the process the energy is released in the form of a photon (phosphorescence) or transferred to adjacent oxygen molecules (quenching). Therefore, the decay in the fluorescence will be proportional to the amount of oxygen molecules surrounding the phosphor, where more oxygen will result in increased quenching and a faster fluorescence decay. This method offers tremendous advantages over O_2 microelectrode based approaches. Since it is an optical based approach, it allows for oxygen measurements as long as the region of interest can be visualized and as long as the phosphor is present in the region of interest. The most commonly used phosphor is albumin-bound palladium-porphyrin, which after intravenous injection, is readily present in the microcirculation as well as in the surrounding tissues, allowing for both intravascular and perivascular PO_2 measurements. Much like O_2 microelectrode measurements, PQM measurements are often confined to a very small region-of-interest, requiring multiple measurements in order to cover a wide region of the microcirculation. Furthermore, the palladium-porphyrin phosphor often leads to long term toxicity, therefore the PO_2 measurements can only be carried out acutely, preventing the long term monitoring of the oxygen dynamics. Finally, it is also known that the excitation of the phosphor leads to a certain amount of oxygen consumption, which can affect the measurements to a certain extent. These limitations are absent from a HSI based approach.

Oxymetry

Microspectrometry, also known as oxymetry, has been widely used for the study of the relative amounts of oxy- and deoxy-Hb present in the blood samples [53]. In fact, oxymetry is one of the most commonly used methods for the non-invasive measurement of oxygen saturation in clinical settings, by means of pulse oxymeters [54]. This approach is the most similar to HSI, as it uses the changes in the spectral properties of Hb when bound to oxygen to determine the changes in Hb O_2 saturation. HbO_2 can be related to changes in PO_2 by means of the Hb dissociation curve. This approach has been employed in the microcirculation by numerous research groups in the form of single and two-point measurements [55, 56]. Unlike HSI which makes use of the measurement of the spectral properties of Hb at multiple wavelengths, oxymetry only makes use of two measurements, one at a wavelength with significant differences bwteen oxy- and deoxy-Hb, and one at an isosbestic wavelength, where the optical density of oxy- and deoxy-Hb is the same. Then, making use of Beer-Ambert's law, the relative abundances of oxy- and deoxy-Hb can be found, yielding the Hb O_2 saturation. Oxymetry can be thought of as HSI in its most primitive form. The use of only two wavelengths makes oxymetry extremely sensitive to scattering and instrument noise during measurements. It also lacks any sort of spatial resolution, as the measurements are often carried out in a single region-of-interest in which a spectrophotometer is focused.

2.2.2 Hyperspectral Imaging for Intravascular Oxygen Measurements

Understanding the way intravascular O_2 measurements have been traditionally done one can see the advantages of using HSI. The most clear advantage is the ability to combine high-throughput measurements with spatial resolution. All of the other approaches are often confined to single-point measurements, requiring multiple

measurements to be performed in order to acquire sufficient information about the oxygenation state of the region-of-interest. Furthermore, while these measurements can often be superimposed with images taken of the measured region, they often require additional imaging approaches, lengthening the measurement process. With the exception of oxymetry, the other approaches also require some sort of interaction with the measure region. In the case of O_2 microelectrodes, the electrode needs to be placed as close to the measurement region as possible, and a perfusate must be used in order to allow for a controlled environment. In the case of PQM, the excitation of the palladium-porphyrin leads to a certain level of oxygen consumption in addition to the tissue toxicity associated with the palladium-porphyrin itself.

The literature surrounding the use of HSI for intravascular oxygen measurements has been dominated by oncological and neurovascular applications. Furthermore, much of the research has been done by the same research groups, using very similar techniques and HSI modalities.

In the study of brain microvasculature and hemodynamics [57] provides a comprehensive review of the current state of the literature. As shown in Table 1 of [57], it is evident that the majority of the HSI approaches for the study of the brain microvasculature involve the use of either spectral scanning or snapshot approaches, with a single study carried out in the late 90s by Malonek et. al. [58] which used a spatial scanning approach. The predominant use of spectral-scanning approaches lies on the simplicity of the approach, as it does not really require large moving parts, as the spatial-scanning approach does. However, this severely limits the spatial resolution of the approach, constraining the imaging to a small region that is highly dependent on the detector size and the lens magnification.

Intravital microscopy studies in peripheral window chamber models, such as dorsal skinfold window chambers, follow a similar trend, with the vast majority of the approaches involving the use of spectral scanning HSI approaches. At this point, there has not been a comprehensive review of what is currently available in the lit-

erature for this specific HSI application. The technique was originally pioneered by Sorg et. al. [25] for use in the study of tumor microvasculature and hypoxia development in a mouse dorsal window chamber model. The animal model consisted of a 4T1 mouse mammary carcinoma implanted inside the viewing region of the mouse dorsal window chamber. The imaging system consisted of a LCTF based spectral scanning system with a 5nm spectral resolution, a spectral range of $500-575$nm and a field-of-view of 2×2mm. In addition to measuring the spectra of hemoglobin, they also used a fluoresence excitation-emission bandpass filter for detecting the emission of green-fluoresence protein (GFP) bound to a HIF-1 transcription factor. The combination of the HSI of the Hb O_2 saturation and the fluoresence imaging of the GFP, allowed to visualize tumor hypoxia in terms of the tumor microvasculature and the internal tumor sensing environment. The results were promising and demonstrated a successful use of HSI for the monitoring of intravascular Hb O_2 saturation, which had not been done before.

Following this preliminary study by Sorg et. al. [25], the technique was further explored by colleagues and others, but preserving much of the original methodology. Wankhede et. al. [59] used the same system for the study of the effects of thromboses and anastomoses in the microvascular oxygenation. They acquired 2×2mm regions of the window chamber every 3 minutes in the presence of thromboses to study their effects on the intravascular O_2 dynamics. Hanna et. al. [60] implemented a very similar system for the study of the lung microvasculature in a novel intravital lung-chamber preparation. In this study the HSI system was also coupled with a fluorescence imaging system which allowed for the measurement of fluorescently labeled red blood cells in order to calculate blood flow in conjunction with Hb O_2 saturation. Choe et. al. [61] used the same technique as [25] for tumor microvasculature measurements as well as macrophage colocalization inside the window chamber. They acquired 2×2mm images along the entirety of the window chamber. Each image took approximately 12 seconds to acquire, with 12 images

required to cover the entire window chamber yielding about 1.5 minutes per image. The images were acquired every 6 hours for analysis. This is the only study that uses whole chamber imaging, but it is done in a discontinuous fashion, through individual image stitching. Zhong et. al. [62] also used the same system for the study of the effects of radiation in the tumor and surrounding microvasculature. He used a wider field of view generating $6x6$mm imaging regions at the expense of decreased spatial resolution when compared to previous implementations of the system. Other similar implementations of the LCTF spectral scanning system originally proposed by Sorg et. al. [25] are summarized in Table 2.2.

In addition to the predominantly used LCTF spectral scanning systems, Hendargo et. al. [63] proposed the use of a snapshot based system. Althrough it falls under the MSI realm, it is still worth mentioning due to its superior temporal resolution when compared to the other approaches. The system consisted of a series of beam splitters and optical filters which generated 4 different projections of the field of view at 540, 560, 580 and 610nm. Since it is a snapshot based approach, all 4 spectral bands were acquired at the same time, having an acquisition time of 0.5s. This proved useful because velocity measurements in slow flowing arterioles and venules was calculated using information from one of the spectral bands. The short acquisition time also allowed the study of hypoxia and reoxygenation dynamics in an almost continuous fashion, but due to the limited imaging region, only a single arteriole-venule pair was analyzed. Styp-Rikowska et. al. [64] also used spectral scanning approach, but instead of using a LCTF, they used a varying monochromator that allowed to acquire images at different wavelengths which were subsequently converted into a hypercube. The acquisition lasted approximately 30s and consisted of an imaging window of 0.67×0.5mm. The measurements were done in the rat mesentery and in mouse dorsal skinfold window chamber models. In addition to spectrally measuring the Hb O_2 saturation, they also measured the total Hb concentration.

In summary, it seems that the use of HSI for the *in vivo* study of the microcirculation has been mostly targeted towards tumor microvasculature studies. Some studies generated timecoure data of oxygenation dynamics, but they were done at either long timescales, or in a very small number of vessels due to spatial resolution limitations. Therefore, there seems to be a lack of studies that address other key physiological phenomena and compounds that can, and should be, studied at the level of the microcirculation such as hemorrhagic shock. Previous HSI based hemorrhagic shock studies used changes in skin and internal organ color, but did not involve direct intravascular oxygen measurements [27]. Furthermore, by an overwhelming majority, the HSI modality of preference was a LCTF-based spectral scanning system, which might be ideal for small scale measurements of tumors and the perivasculature in window chamber models, but lacks the spatial resolution to properly understand the oxygenation state of the remainder of the window chamber, which can provide key insights towards the general state of the microcirculation. It is true that stitching approaches such as the one presented by [61] allow for a whole-chamber visualization, they lack the temporal resolution for the study of oxygen dynamics during acute conditions such as hypoxia onset, reoxygenation, ichemia-reperfusion and hemorrhagic shock.

Table 2.2: List of research articles that used HSI for the study of *in vivo* window chamber animal models. **FOV** corresponds to the width of the imaged field-of-view. **Modality** corresponds to the HSI modality used in the study. When appropriate, the type of dispersive element is also mentioned. **Acquisition Time** corresponds to the amount of time required to acquire a single hyperspectral image. **Timecourse** represents whether subsequent images are acquired, and how often those images are acquired. **Spectral Range** corresponds to the range of wavelengths of the recorded spectral bands. **Spectral Resolution** corresponds to the separation between subsequently acquired spectral bands. **Measurements** Corresponds to the measurements carried out with the HSI, as well as any other additional measurements carried out with coupled imaging modalities.

Reference	FOV	Modality	Acquisition Time	Timecourse	Spectral Range	Spectral Resolution	Measurements
Sorg et. al. [25]	2x2mm	LCTF Spectral Scanning	Not reported	No	500-575nm	5nm	Mouse microvasculature and tumor hypoxia in dorsal window chamber
Hanna et. al. [60]	2x2mm	LCTF Spectral Scanning	Not reported	No	500-590nm	10nm	Lung window chamber microvascular hemoglobin oxygen saturation. Velocity was measured with labeled RBCs and conventional microscopy
Rasul et. al. [65]	4x4mm	LCTF Spectral Scanning	Not reported	No	520-620nm	10nm	Mouse dorsal skinfold window chamber tumor hypoxia dynamics
Agarwal et. al. [66]	2x2mm. Whole window images acquired through image stitching	LCTF Spectral Scanning	13s per region. Entire chamber in 2.6min.	Every 20s	500-575nm	5nm	Mouse dorsal skinfold window chamber tumor hypoxia dynamics over time.

Reference	FOV	Modality	Acquisition Time	Timecourse	Spectral Range	Spectral Resolution	Measurements
Wankhede et. al. [59]	2x2mm	LCTF Spectral Scanning	13s	Every 3min	500-575nm	5nm	Mouse microvascular malformations and thrombus development
Skala et. al. [67]	1x1mm	LCTF Spectral Scanning	Not reported	Every 6 hours	500-610nm	10nm	Mouse tumor microvascular oxygenation. Doppler OCT was used to measure blood flow
Lee et. al. [68]	3x3mm	LCTF Spectral Scanning	13s	Daily	500-575nm	5nm	Mouse microvascular malformations and tumor oxygenation. Blood flow was monitored through fluoresence imaging.
Zhong et. al. [62]	6x6mm	LCTF Spectral Scanning	Not reported	No	520-620nm	10nm	Mouse tumor oxygenation before and after radiation treatment.

Reference	FOV	Modality	Acquisition Time	Timecourse	Spectral Range	Spectral Resolution	Measurements
Sorg et. al. [69]	2x2mm	LCTF Spectral Scanning	13s	Every 3min	500-575nm	5nm	Mouse microvascular malformations and longitudinal gradients in tumors
Palmer et. al. [70]	4x4mm	LCTF Spectral Scanning	31s for boron nanoparticles. Not reported for Hb saturation	Every 7.5min	520-620nm for Hb Sat, 425-575nm for boron nanoparticles	5nm for boron nanoparticles, 10nm for Hb sat	Combination of boron nanoparticle and Hb saturation measurements. Boron nanoparticle emissions allow for calculation of tissue oxygen tension maps
Fontanella et. al. [71]	2x2mm	LCTF Spectral Scanning	13s	No	500-575nm	5nm	An automated algorithm that combines multiple imaging modlaities to determine blood velocity, Hb saturation and morphological features

Reference	FOV	Modality	Acquisition Time	Timecourse	Spectral Range	Spectral Resolution	Measurements
Choe et. al. [61]	2x2mm. Whole window images acquired through image stitching	LCTF Spectral Scanning	13s per region. Entire chamber in 2.6min.	Every 6hrs	500-575nm	5nm	Mouse dorsal skinfold window chamber tumor oxygenation with macrophage co-localizatiom
McCormak et. al. [72]	1.5x1.5mm	LCTF Spectral Scanning	13s	Daily	500-600nm	4nm	Tumor microvascular oxygenation in response to trastuzumab chemotherapeutic treatment
Styp-Rekowska et. al. [64]	670x500um	Digital Grating Switching Monochromator Spectral Scanning	30s	No	500-598nm	2nm	Mouse mesentery and dorsal skin oxygenation. Total hemoglobin was also spectrally measured.
Hendargo et. al. [63]	4x4mm	Snapshot	0.5s	Every 0.5s	4 wavelengths: 540, 560, 580 and 610nm	Multispectral resolution	Measurement of oxygen dynamics and velocity of blood

Chapter 3

Hyperspectral Wide-Field-Of-View Imaging to Study Vascular Microcirculation Dynamic Changes During Hypoxia

3.1 Introduction

Hyperspectral imaging (HSI) has gained recent popularity in biomedical research applications. The ability to process increasingly larger amounts of data and the relatively easy accessibility to benchtop HSI systems has allowed researchers in recent years to develop many HSI applications, which range from the experimental to clinical setting[6]. The ability of HSI in determining the relative concentrations of biologically relevant chromophores (i.e. hemoglobin and its derivatives) in a non-invasive and non-destructive way, makes HSI an ideal tool for the study of microvascular and angiogenic processes, including oxygen delivery and vascular morphology.

In the microcirculation, specifically in dorsal window chamber models, HSI

usage has been focused in the study of tumor oxygen distribution [70, 72, 25] and angiogenesis [73, 74]. These studies often involve customized microscope setups which are based on either snapshot or spectral scanning HSI [67, 63]. Many of these studies, since they are primarily focused in studying the regions near the tumor, often ignore the oxygenation and morphological changes that occur in adjacent areas of the microcirculatory network. Although dorsal window chamber diameters are on the order of 12 to 15mm, depending on the species, previous HSI studies image regions ranging between 2mm and 5mm, which correspond to less than 30% of the chamber field of view imaged at any given time [63, 25, 70]. This prevents the use of HSI to study larger scale phenomena such as microcirculatory network dynamics and its regulation. Alternatively, instead of using a fixed field of view as in spectral scanning or snapshot HSI, a linear scanning, or pushbroom, HSI system could be used. In these systems a single fixed length line of the image is acquired at any given time and the field of view is determined by the length of the acquired line and the scanning distance, allowing for more flexibility in the size of the image in the scanning axis at the expense of increased acquisition time. Pushbroom HSI systems have been previously used for saturation and microcirculation studies in the brain and the eye of cats and non-human primates respectively [58, 75], but not in the more common murine window chamber model, where either spectral scanning or snapshot HSI systems are more commonly used under the premise of being faster.

In this study, an off the shelf, benchtop, linear scanning hyperspectral imaging system was used in order to acquire wide-field-of-view images in the horizontal direction of hamster dorsal window chambers. Images were taken as the animals were subjected to hypoxia and reoxygenation to obtain the dynamic changes in hemoglobin (Hb) oxygen (O_2) saturation and microvessel diameter of the entire microvascular network. The acquired Hb O_2 saturation maps were compared against phosphorescence quenching microscopy (PQM) measurements of oxygen tension (pO_2) in the same vessels.

3.2 Methods

3.2.1 Animal Preparation

Animal handling and care followed the NIH Guide for the Care and Use of Laboratory Animals and the experimental protocol was approved by the local animal care committee. Studies were performed in 55 - 65 g male Golden Syrian Hamsters (Charles River Laboratories, Boston, MA) fitted with a dorsal window chamber. Details about hamster chamber preparation can be found in previous studies [76].Briefly, animals were anesthetized with a 50mg/kg injection of sodium pentobarbital. Dorsal hair was removed and sutures were used to lift the dorsal skin from the back of the hamster, where a titanium frame, consisting of two symmetric sides with a 15mm circular window, was positioned. On one side, within the circular window, layers of the epidermis were removed until the blood vessels in the underlying dermis could be observed. The exposed tissue was then covered with a glass coverslip. Animals were allowed two days to recover prior to performing the experiments.

3.2.2 Hyperspectral Image Acquisition

A Pika-L hyperspectral imaging system with a mounting tower, linear translation stage and stabilized lighting assembly (Resonon, Bozeman, MT) was used for image acquisition. The Pika-L system has a spectral range between 390-1020nm, a spectral resolution of 2.1nm, and a spatial resolution of 900 pixels per line. The lighting assembly consisted of 4 broadband halogen bulbs angled at 45^o towards the imaged region. All 4 bulbs were controlled simultaneously through an Arduino controlled power relay (Digital Loggers, USA), which allowed to synchronize the image acquisition with the lighting in order to prevent excessive heat exposure in the animal during the experiment. A variable magnification VariMagTL telecentric lens (Edmund Optics, Cupertino, CA) was used as an objective with a maginification

of approximately 2.5X. The variable magnification allowed for minor adjustments in the field of view without the need of vertically translating the imaging stage. Images were taken at a continuous linear scanning speed of $0.8mm/s$, a framerate of $218Hz$ and an integration time of $4.4ms$. A total of 2900 lines were scanned in the horizontal direction to cover an entire horizontal region of the chamber with each image (Figure 3.1A). Therefore, each image consisted of a $2900 \times 900 \times 300$ hypercube, which resulted in an image size of $15mm \times 4.5mm$ with a spatial resolution of $5\mu m/pixel$ in the spatial dimensions and wavelengths between 390-1020nm, with a spectral resolution of $2.1nm$ in the spectral dimension. Each image was acquired in 14.5 seconds, with 20 more seconds required for image transmission and storage onto the computer. While the transmission and storage time are limiting factors in this case, the image acquisition time is comparable to the $12.5s$ per image reported in [72], and the $31s$ per image reported in [70], both of which used spectral scanning HSI. It is unclear, however, whether these reported times include image transmission and storage, or not. Furthermore, previous studies only cover spectral ranges of about $150nm$, and 30% of the chamber in any direction, whereas in the proposed approach a spectral range of $600nm$ is covered, with 100% of the chamber covered in the horizontal direction. All images were acquired through a customized Python script that, simultaneously, interfaced with the light source power relay through an Arduino Uno microcontroller, and coordinated image acquisition through the Spectronon hyperspectral acquisition software (Resonon, Bozeman, MT).

3.2.3 Hyperspectral Image Preprocessing

All analyses were done through custom Python scripts in a personal Laptop computer with Windows 10, 16Gb RAM and a 2.4GHz processor. After acquisition, images were truncated and resampled in the spectral domain between $500 - 590nm$, with a spectral resolution of $2nm$. The spectral resampling allows the spectral sam-

pling of the hypercube to match the spectra sampling of the reference spectra used to generate the HbO_2 saturation maps. This reduced each image into a $2900 \times 900 \times 45$ hypercube. To correct for impulse noise, such as salt-and-pepper noise, a 2D mean filter with a 5×5 kernel was applied in the spatial domain at each spectral band. To optimize the mean filter implementation across all spectral bands, a $5 \times 5 \times 45$ kernel was used instead of the conventional 2D kernel. Each component in the third dimension of this 3D kernel consisted of a 5×5 matrix, with all elements having a value of $1/25$. This allowed to compute the convolution of the kernel with the image simultaneously at every spectral band, taking advantage of Python's broadcasting functionality. Following the mean filter, a Savitzky-Golay filter with a 4th order polynomial and a window length of 23 was applied across all spectral bands for a given pixel spatial location [77].

After filtering, the $560nm$ band was used in order to create a vessel mask through reflectance intensity thresholding. Other approaches for generating vessel masks have been proposed, such as the use of Gabor filter banks and connectivity based approaches [63, 78]. However in the proposed application, only similar or worse performance was obtained with these apporaches when compared to simple intensity thresholding. The intensity thresholding approach is based on the fact that dermal tissue reflectance is larger than vessel reflectance at the $560nm$ spectral band. The threshold value was determined at one standard deviation below the mean intensity of all the pixels at the $560nm$ spectral band. Subsequently, after the vessel mask was obtained, the spectral dimension was rescaled to have a minimum reflectance of 0 and a maximum reflectance of 1 at each pixel. That is, the spectra at each spatial location ranged between 0 and 1. Essentially, this spectral rescaling serves as a per-pixel scattering correction factor, which brings the reference and measured spectra to the same range, easing the spectral unmixing process. Traditional approaches make use of an effective scattering coefficient for the sample in question, in this case, the effective scattering coefficient for hamster skin would be used. However,

the effective scattering coefficient, while wavelength dependent, is often assumed to be the same across the entirety of the sample. This is not always the case, as there might be inhomogeneous illumination across the sample. Furthermore, for the dorsal window chamber, different types of connective tissue will also be present within the field of view, causing the assumption of a homogeneous scattering function to be further invalidated. Instead, using the spectral rescaling approach, a pixel dependent scattering correction is applied across the entire sample, and since the reference spectra is also rescaled with the same approach, the spectral unmixing is significantly improved.

3.2.4 Hemoglobin Oxygen Saturation Map

Reference deoxy- and oxy-hemoglobin reflectance spectra were used as the pure spectral endmembers during spectra unmixing. The reference oxy-hemoglobin spectra was acquired from rat hemoglobin taken from hemolized blood of a single donor. The reference deoxy-hemoglobin spectra was acquired from the same hemoglobin sample treated with excess sodium ditionite [79]. Absorbance was measured with a benchtop spectrophotometer (Ocean Optics, FL) sampled at $2nm$ intervals between $500-600nm$. Conversion between measured absorbance and reflectance was done through the approximation $R(\lambda) = log\,(1/A(\lambda))$, where $R(\lambda)$ corresponds to the reflectance at a given wavelength, λ, and $A(\lambda)$ corresponds to the absorbance at that same wavelength. Using a modified version of Beer's law, as described extensively before [63, 25, 70], the reflectance at a given pixel can be written as

$$R(\lambda) = b_o + C_{Hb}R_{Hb}(\lambda) + C_{HbO}R_{HbO}(\lambda) \tag{3.1}$$

where C_{Hb} and C_{HbO} correspond to the relative concentrations of deoxy- and oxy-hemoglobin respectively, and b_o is a constant term that accounts for variation in intensity from the source. The commonly used scattering term is not necessary due to the spectral rescaling of the image described previously. The above relationship

was formulated as a least squares problem expressed as

$$C = \left(X^T X\right)^{-1} X^T Y \tag{3.2}$$

where X is an $M \times N$ matrix with M corresponding to the number of spectral bands, and $N = 3$, where the first two columns correspond to $R_{Hb}(\lambda)$ and $R_{HbO}(\lambda)$, and the third column is populated by ones. Y is an $M \times K$ matrix corresponding to the two dimensional reshaped hypercube with K corresponding to each pixel in the spatial dimension, and M to each band in the spectral dimension. Consequently, C is then an $N \times K$ matrix populated by the respective C_{Hb}, C_{HbO} and b_o for each pixel in the K dimension. This formulation allows for an efficient vectorized calculation of the relative doxy- and oxy-hemoglobin abundances. Finally, the hemoglobin saturation at any given pixel was then found by $Sat = C_{HbO}/(C_{Hb} + C_{HbO})$.

3.2.5 Automated Diameter Measurement

Automatic diameter measurement was performed in user selected rectangular regions of interest (ROIs). For automatic vessel diameter estimation, the boundaries of the vessel were first extracted through a Canny edge detection algorithm [80]. After edge detection, the location of the points corresponding to the edges were subjected to a density-based spatial clustering of applications with noise (DBSCAN) unsupervised clustering algorithm [81], under the assumption that each boundary (i.e. left or right boundary) will belong to a different cluster. After the left and right boundary clusters were determined, the centroid of each cluster was calculated, and the distance between both centroids was used as the average diameter of the vessel within the specified ROI. The robustness of DBSCAN prevents extraneous edge points from interfering in the calculation of the cluster centroid.

3.2.6 Phosphoresence Quenching Microscopy

The resulting saturation maps were compared to direct measurements of intravascular pO_2 using phosphoresence quenching microscopy (PQM) following methods described in previous studies [50, 82]. Briefly, PQM is capable of determining intravascular pO_2 based on the O2-dependent quenching of albumin-bound polyporphyrin upon pulsed light excitation. The decay in the fluorescense after light excitation is proportional to the pO_2 in the vessels. After intravenous injection of polyporphyrin into the animal ($0.05\mu L$), PQM measurements of the pO_2 were done in regions of interest (ROI) of about $15\mu m$ radially and $40\mu m$ longitudinally, centered at locations such as those shown by the arrows in Figure 3.1B. pO_2 measurements were converted to Hb O_2 saturation values the hamster blood Hb O_2 dissociation curve (Hill curve) [83], and were compared to the saturation values obtained through the proposed HSI methodology, determined by the average saturation in a ROI centered in the same place as the one used for PQM measurements, but with the entire radial component of the vessel and $0.5mm$ in the longitudinal component.

3.2.7 Hypoxia and Reoxygenation Protocol

Hamsters were subject to hypoxia and reoxygenation following an approach similar to previous studies [84]. Briefly, the animals were restrained in an hollow acrylic tube with a sideways slit through which the chamber could protrude. The opening of an inflow tube, was connected to the restraining tube, and compressed room air at 21% oxygen was allowed to flow for 10 minutes prior to the beginning of the experiment. After 10 minutes, the animals were subjected to 8% oxygen for 9 minutes and recovered for 9 minutes with compressed room air at 21% oxygen. Hyperspectral images of the chamber were taken at the beginning and every 45 seconds for a total of 11 images per stage (i.e. 11 for hypoxia and 11 for hypoxia reoxygenation). After image acquisition, images were processed following the pro-

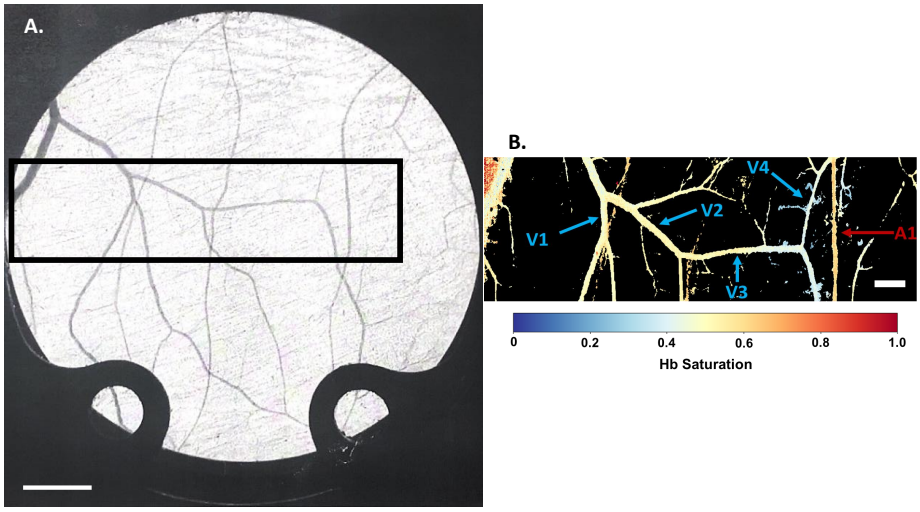

Figure 3.1: **A.** Grayscale image of the dorsal skinfold window chamber. Scale bar corresponds to $2.14mm$. The black rectangle represents the analyzed region. **B.** Resulting hemoglobin saturation map with venules (V) and arterioles (A) labeled. Scale bar corresponds to $1mm$. Arrows point to the center of the rectangular region of interest analyzed for comparison with the PQM measurements, and where saturation and diameter measurements were performed.

posed methodology. Despite having continuous saturation maps, discrete ROIs were selected in order to quantify the results. A total of 5 arteriole and 8 venule ROIs were selected in each preparation, allowing for 20 arteriole and 32 venule saturation measurements at each hypoxia/reoxygenation timepoint.

3.2.8 Statistical Analysis and Curve Fitting

The r^2 value of the spectral least-squares fit at every pixel was calculated within the same custom Python script using the relationship,

$$r^2 = 1 - \frac{\sum_\lambda \left(R(\lambda) - \bar{R}\right)^2}{\sum_\lambda \left(R(\lambda) - \hat{R}(\lambda)\right)^2} \tag{3.3}$$

where, at any given pixel, $\bar{R}$ corresponds to the mean value of the reflectance spectra, $R(\lambda)$ corresponds to the reflectance spectra at wavelength λ, and $\hat{R}(\lambda)$ corresponds to the spectra resulting from the least squares fit at wavelength λ.

For the HbO_2 saturation and diameter timecourses during hypoxia and reoxygenation, datapoints are presented as mean $\pm$ standard deviation. The timecourses were curve fitted using GraphPad Prism 7 (GraphPad, San Diego, CA), making use of the built-in sigmoidal and exponential association and decay equations. Goodness of fit was assessed through r^2 analysis. The PQM derived saturation measurements were compared with the HSI derived measurements by comparing the linear relationship between the two, to the relationship between two identically performing measurement systems (a slope=1 line).

3.3 Results

The biggest advantage of using a spatial scanning HSI system is the ability to image large fields of view. For microcirculation studies this proves particularly useful, as it allows for the imaging of a wide enough region to quantify the global state of the microcirculation at any given time. Figure 3.1A shows an example of an imaged region with respect to the rest of the chamber, and Figure 3.1B shows the resulting saturation map, after processing with the proposed methodology. The arrows pointing towards arterioles and venules in Figure 3.1B show examples of the center of the ROIs used for saturation, diameter and PQM analysis. The r^2 value of the least-square fit at every pixel, for all analyzed HSIs, was at least 0.85, with the majority above 0.95.

3.3.1 Image Processing

The output of every stage of the image processing pipeline, for a single HSI, is shown in Figure 3.2. Observing the original RGB reconstructed image, it can be

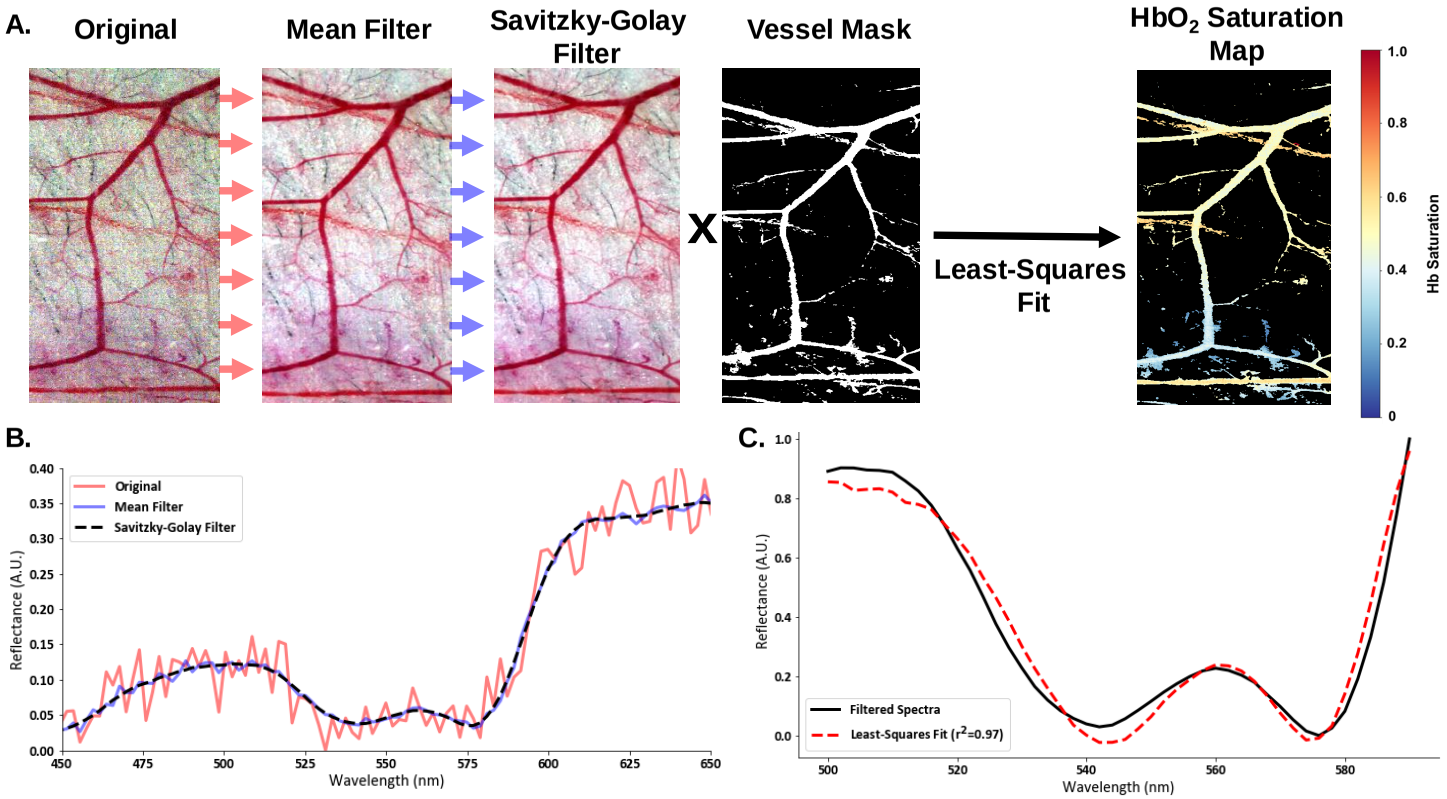

Figure 3.2: **A.** RGB reconstructed images from HSI right after acquisition, after implementation of the mean filter, after implementation of the Savitzky-Golay (SG) filter, after intensity thresholding and after least-squares fitting for the generation of the HbO_2 saturation map. Note how the vessel mask is multiplied by the SG filtered image, eliminating the presence of tissue in the final image. **B.** Single pixel spectrum in the original image, after the mean filter and after the SG filter. **C.** Final filtered spectra and corresponding least-squares fit ($r^2 = 0.97$) for the same pixel shown in **B.**

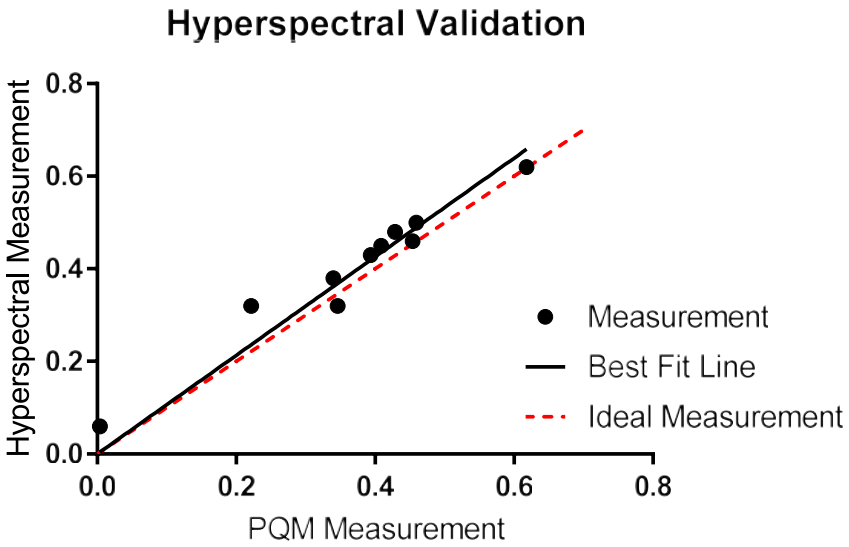

Figure 3.3: Scatterplot of PQM derived and hyperspectrally derived saturation values for 10 vessels measured accross 2 different animals. The black line represents the 0-crossing best fit line for the measurements (RMSE=0.043), and the dashed red line represents the expected best fit line if the measurements were to match exactly.

seen how there is a significant amount of salt-and-pepper noise present in the image. The presence of noise is even more noticeable in the spectral dimension, as shown in in Figure 3.2B, where the spectrum of a single pixel is shown. After application of the mean filter, the salt-and-pepper noise present in the image was significantly reduced, as was the noise in the spectra. Finally, the Savitzky-Golay filter seems to have an indistinguishable effect in the image after the mean filter. However a greater effect is seen in the spectra, where it seems to generate a much smoother final spectra. The multiplication of the binary vessel mask and the HSI, generates a tissue-free HSI, over which the spectral unmixing can be performed through the least-squares approach proposed. Figure 3.2C shows the resulting least-squares fit on the filtered spectra shown in Figure 3.2B, which had an r^2 value of 0.97.

3.3.2 PQM Validation

A scatterplot of PQM and hyperspectrally derived saturation measurements in the vessels shown in Figure 3.1B (n=10 vessels), is presented in Figure 3.3. The zero-crossing best fit line had a root mean squared error (RMSE) of 0.043, and a slope of 1.065, compared to the slope of 1 in the ideal measurement line.

3.3.3 Hypoxia and Reoxygenation Timecourse

Figure 3.4 shows the resulting saturation maps acquired at baseline, after hypoxia, and at 1.5, 2.25, 3 and 8.25 min during reoxygenation. The HbO_2 saturation timecourse, as measured at specific arteriole and venule ROIs is shown in Figure 3.5A-B shows the resulting exponential decay in the HbO_2 saturation during hypoxia. The fitted exponential decay for the venules has a τ value of 0.55 compared to a τ of 0.70 for arterioles, suggesting a faster decay for the venules. Figure 3.5B shows the reoxygenation HbO_2 saturation timecourse, where the arteriole roxygenation is modeled as an exponential recovery, and the venule reoxygenation is modeled as a sigmoid.

Diameters of the ROIs analyzed previously were measured using the proposed approach during hypoxia and reoxygenation. Their respective timecourses are shown in Figure 3.6. The final diameter during hypoxia was used as the initial diameter during reoxygenation. During hypoxia, arterioles vasoconstricted by approximately 20% of their initial value, and followed an exponential decay. Venules increase in diameter by approximately 10% following an exponential recovery. On the other hand, during reoxygenation, arterioles followed a sigmoidal increase in diameter of 40% relative to the end of hypoxia. During reoxygenation, venules followed a sigmoidal decay of 10% relative to the end of hypoxia. These results show that during hypoxia and reoxygenation the changes in diameter are grater for the arterioles than the venules.

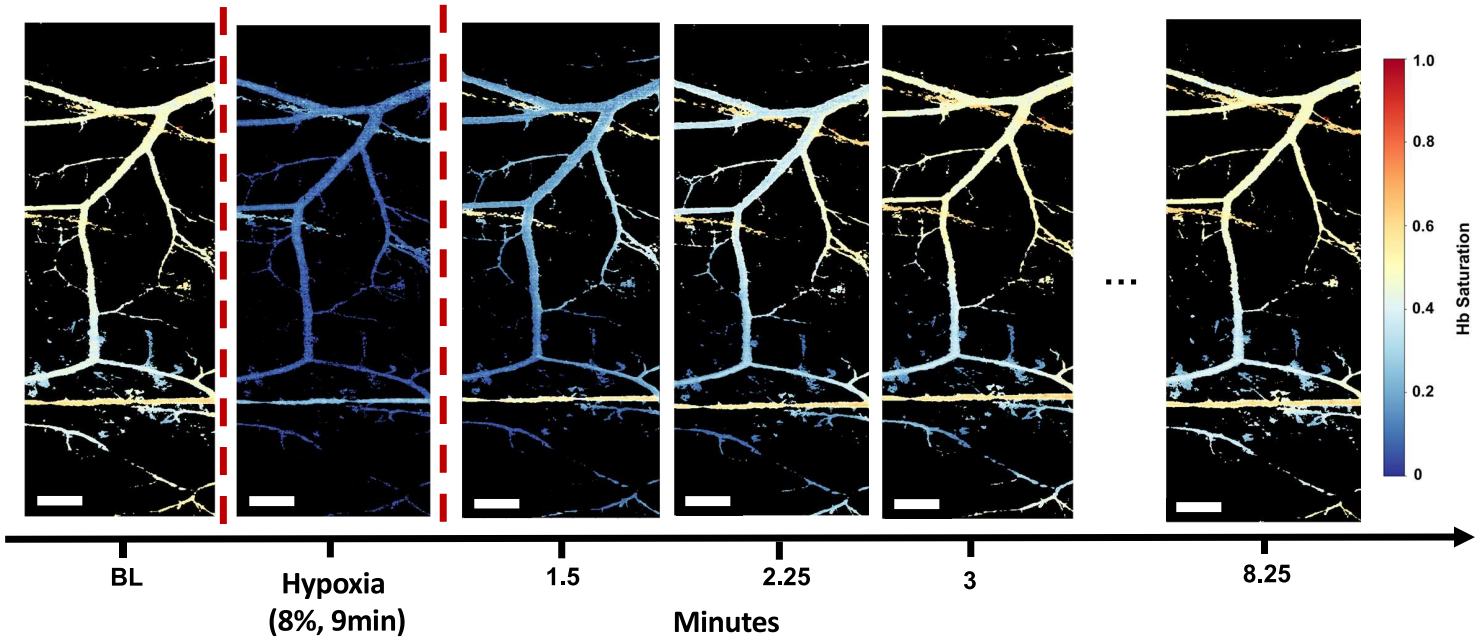

Figure 3.4: **A.** Saturation maps acquired at baseline, after hypoxia, and at different time-points during reoxygenation (1.5, 2.25, 3 and 8.25 min). Scale bar $1mm$.

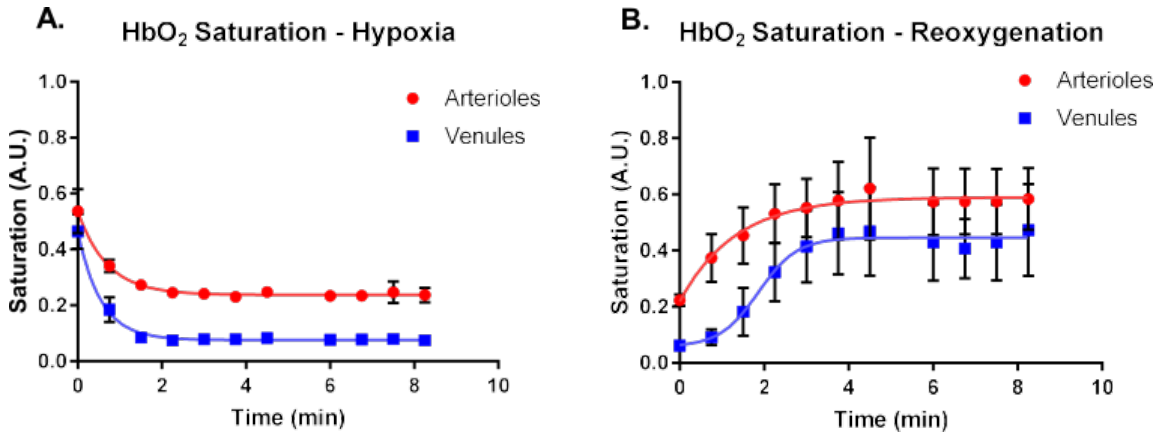

Figure 3.5: **A.** and **B.** show saturation changes during hypoxia and reoxygenation in arterioles and venules, respectively. In **A.**, lines represent non-linear exponential decay fits ($r^2 = 0.91$ for arterioles and $r^2 = 0.96$ for venules). In **B.**, lines represent non-linear fits, with an exponential recovery for arterioles ($r^2 = 0.98$), and a sigmoidal recovery for venules ($r^2 = 0.98$).

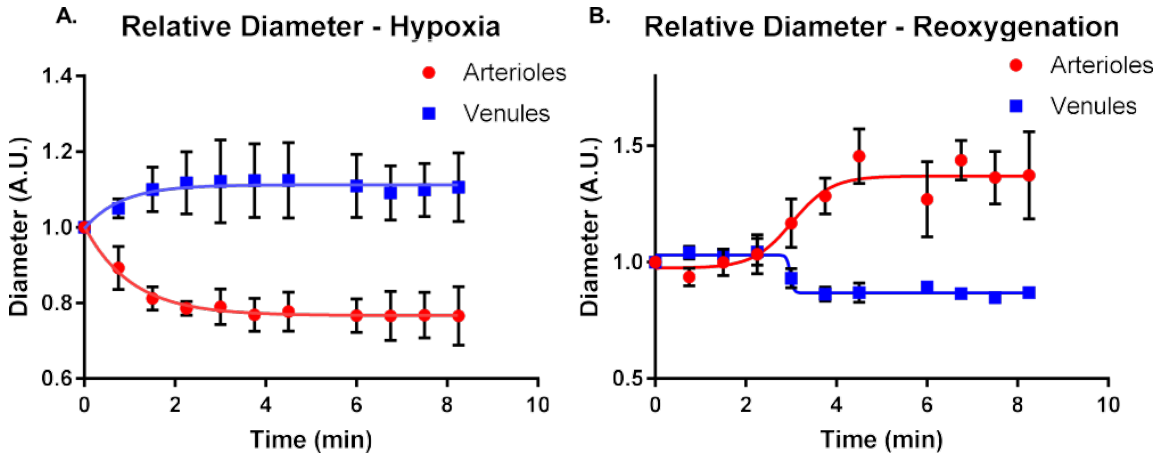

Figure 3.6: Diameter changes during hypoxia **A.**, and reoxygenation **B.** in arterioles and venules. In **A.**, lines represent non-linear fits, with an exponential decay for arterioles ($r^2 = 0.99$), and an exponential recovery for venules ($r^2 = 0.88$). In **B.** lines represent non-linear fits, with a sigmoidal recovery for arterioles ($r^2 = 0.75$), and a sigmoidal decay for venules ($r^2 = 0.86$).

3.4 Discussion

The results presented in this study indicate that hyperspectral wide-field-of-view imaging with the proposed methodology can detect dynamic changes in HbO_2 oxygen saturation and vessel diameter during hypoxia and reoxygenation.

Comparison of the PQM measured saturation and the HSI measured saturation suggests small differences between the two approaches across a wide range of HbO2 saturation values, which suggests consistency in the HSI methodology. To our knowledge, this is the first time a HSI approach has been validated through an *in vivo* approach in the microcirculation. The difference in slope between the measurement best-fit and the ideal measurement suggests that a small linear correction factor could suffice to eliminate most measurement discrepancies between the two approaches. It is worth noting, however, that the errors seem to increase as saturation decreases, or as the relative abundance of oxy-hemoglobin approaches zero. This is a limitation of the HSI measurement approach, since the least-square fit seems to underperform when fitting pure spectra, unless the spectra exactly matches the reference spectra. Therefore, the performance of the fit is better if the relative abundances of oxy- and deoxy-hemoglobin are larger than zero, than if they are closer to zero. This behavior is likely to be due to the fact that the error function will increase when the abundances of either oxy- or deoxy-hemoglobin species decrease. In the presence of pure, or almost pure absorbances of either oxy- or deoxy-hemoglobin (i.e. fully oxygenated, or fully deoxygenated blood), then the presence of random noise is more detectable as any small deviations from the pure spectra will suggest the presence of the other species. Finally, conversion between the reflectance and absorbance domain is also an approximation, which can increase discrepancies between the reference spectra and the measured image spectra, leading to a larger error during the fit.

The hypoxia and reoxygenation dynamics measured by the wide-field-of-view HSI approach also proved to be consistent with physiological behavior. Hypoxia

timecourse HbO_2 saturation shows a faster decay for the venule saturation than for the arteriole saturation, as shown by the different τ values of the decay. This indicates that as hypoxia is prolonged, most of the O_2 in the blood is delivered to the tissues to compensate for the metabolic demand. This results in less O_2 arriving to the venules at any given time, consequently leading to a faster decay of the venule saturation relative to the arterioles. Differences in the steady state values for arterioles and venules are also noticeable (Figure 3.5A), suggesting the presence of more oxygen in arterioles than in venules at any given time. The reoxygenation timecourse in Figure 3.5B shows interesting dynamics, where the arteriole reoxygenation is modeled as an exponential recovery, whereas the venule reoxygenation is modeled as a sigmoid. This is consistent with previous studies in skeletal muscle [85]. The initial plateau phase in venule reoxygenation is evidence of a delayed recovery of the venules, relative to the arterioles, likely due to the need for the tissue to recover prior to the recovery of the Hb O_2 saturation in the venules. This supports the idea of two "pools" of O_2, in the tissue and in the venules, where the recovery in the venules takes place only when the recovery of the tissue pool has been completed.

The proposed methodology was also capable of determining dynamic changes in microvessel diameter. The results show that in both hypoxia and reoxygenation, the change in diameter is grater in arterioles than in venules. This is consistent with the increased presence of smooth muscle in arterioles. Classically, it is expected for arterioles to dilate during hypoxia in order to allow for the increased blood flow to increase oxygen delivery (e.g. Hypoxia vasodilation) [86]. However, hypoxia vasodilation is mostly observed in vital tissues, whereas connective tissue (e.g. skin) and muscle contract during hypoxia to allow increased O_2 delivery to vital tissue. Relating the HbO_2 saturation and diameter timecourses, one can see that during hypoxia, an exponential decay in saturation, is met with an exponential decay in arteriole diameter and an exponential recovery in venule diameter, both with τ values of approximately twice as those of the Hb O_2 saturation recovery. During reoxygenation,

diameter changes involve sigmoidal responses in both types of vessels. This suggests that while there is a continuous change in diameter during hypoxia, more abrupt changes take place during reoxygenation. A plausible explanation for this behavior during reoxygenation also involves need to replenish the tissue O_2 pool before recovering venular saturation. This study confirms that the saturation in the arterioles recovers fast relative to the venules, since they can be thought of as the main source of oxygen to the tissue. Vital tissues recover their oxygen at the beginning of reoxygenation, therefore, the diameter of the arterioles in the dorsal window, a non-vital tissue, will remain constricted. As the vital tissues recover their oxygen, arterioles in other non-essential tissues will begin to dilate to allow their oxygen to recover. In fact, the arterioles over-dilate by about 10% of their original value in an attempt to compensate for the decreased oxygenation in dorsal window after recovery of the vital-tissue oxygenation. These changes in diameter also reflect the regulatory blood flow changes in the central circulation during hypoxia and reoxygenation.

One limitation of this study is the processing time for the HSI after acquisition. The illustration of the processing pipeline shown in Figure 3.2 provides insight as to how the saturation maps are generated. The average processing time for a single image is approximately 4.5 minutes, with the mean filter and the spectral resampling taking about 2 minutes each, the Savitzky-Golay filter about 8 seconds, and the intensity masking, spectral rescaling and least-squares fit taking less than a second each. These performance times suggest that the most time consuming portion of the processing pipeline is the pre-processing stage, which includes the spatial and spectral filtering as well as the spectral resampling. Future implementations should aim to reduce the need for spectral resampling, by using reference spectra acquired by the same imaging system, or to reduce the need for a mean filter by increasing the detector quality. Alternatively, these post-processing tasks, due to their highly iterative nature, could be parallelized through GPU parallel computing approaches for improved performance.

Although this study only includes hypoxia and reoxygenation, other animal models (e.g. anemia, hemorrhage, etc) can be performed and other animal preparations such as cremaster muscle preparations and cranial windows can be used as a means of expanding the applications of the proposed methodology in those models. Future studies will aim to use the proposed HSI approach to study the morphology and saturation relationships presented in this study in more detail, as well as in dorsal window models during hemorrhagic shock/resuscitation, mild and severe anemia, and in combination with hemoglobin-based oxygen carriers. This latter will aid in understanding the oxygen carrying capacity and the oxygen delivery of novel blood substitutes, when compared to regular blood transfusions, and their implications in the microcirculation.

3.5 Conclusion

The results presented in this study show that spatial scanning wide-field-of-view hyperspectral imaging is can generate HbO_2 saturation maps of the entirety of the window chamber. Furthermore, the imaging approach has sufficient temporal resolution in order to detect dynamic morphological and HbO_2 saturation changes during hypoxia and reoxygenation. The reported system enables microcirculation dynamic functional imaging for broad experimental and clinical applications.

Chapter 4

Modeling Acute Hypoxia Dynamics in Mouse Dorsal Window Chamber Models

In the previous chapter the use of HSI for the study of hypoxia dynamics was illustrated in a hamster window chamber model. In this chapter, the same system will be used to study hypoxia dynamics in a mouse window chamber model. While the approach used is identical to the one described in the previous chapter, mouse models seem to behave differently during reoxygenation. Specifically, the response to hypoxia seems to be different after subsequent hypoxic cycles. Furthremore, during reoxygenation, mice seem to have a transient overshoot in venular, and to a much lesser extent, arteriolar saturation. This transient overshoot behaves similarly to what one would observe in the presence of reactive hyperemia, upon occlusion of a blood vessel. This chapter will explore this behavior and present a simple second order linear system capable of modeling it.

4.1 Introduction

The study of the effects of hypoxia has significant clinical relevance. Conditions that decrease oxygen availability to vital tissues such as hemorrhagic shock and ischemia are common clinical emergencies, whose damage is mostly associated to the effects hypoxia has in the body. The presence of hypoxia often induces a series of cellular and metabolic cascades in an attempt to mitigate the decrease in oxygen supply. Among the metabolic changes, the most prominent one is the increase in anaerobic glycolitic activity [87], which is highly controlled by the upregulation and stabilization of hypoxia inducible factors (HIF) [88]. Another known mechanism resulting from hypoxic insult is the generation of reactive oxygen species (ROS), which has also been tied to the increased expression of HIF [89]. These, as well as other metabolic and signaling cascades, are present to some extent in all mammalian cells [90]. Of particular importance, however, is the response of endothelial cells to hypoxic insult. Endothelial cells are the first line of contact with the hypoxic insult, since they have direct exposure to the blood supply. Through specialized mechanisms such as nitric oxide (NO) release and other still somewhat unclear pathways, endothelial cells vasodilate and vasoconstrict in a preferential manner in an attempt to increase bloodflow towards preipheral tissues [91]. This endothelial hemodynamic response is of key importance in the microcirculation, where the majority of oxygen transport takes place.

Studies of the effects of hypoxia in the microcirculation have been carried out extensively [92, 85]. Common techniques for the measurement of oxygen in the microcirculation and peripheral tissues during hypoxia experiments include O_2 microelectrodes [85] and phosphoresence quenching microscopy (PQM) based approaches [92] in canine skeletal muscle and rat cremaster muscle preparations, respectively. Newer techniques such as hyperspectral imaging (HSI) have also been used for the study of tumor hypoxia and microvasculature in window chamber models [25, 63], and in

the retinal microcirculation of rabbits [38] and non-human primates [75]. Studies in humans using transcutaneous measurements [93] and pulse oximetry [94, 95] have also been done, although they measure volume averaged effects as single microvessel oxygenation can not be assessed through these methods. Many of these studies have presented the intravascular or perivascular changes in oxygen during and after the hypoxic insult. Little focus, however, has been done to attempt to model such responses with a mathematical model.

In this study, HSI of the a mouse window chamber model was used to study hypoxia dynamics after repeated cycles of hypoxia. A mathematical model, based on a second order linear system was developed to fit the observed changes in hemoglobin oxygen saturation (HbO_2) during hypoxia and reoxygenation. Differences in the behavior of arterioles and venules during hypoxia and reoxygenation were assessed using the developed model.

4.2 Methods

The HSI system, the HSI processing pipeline and the animal preparations are identical to those described in Chapter 3, with the exception that uncatheterized C57 mice instead of Golden-Syrian Hamsters were used in this study. Please refer to the corresponding sections in that chapter for more details.

4.2.1 Hypoxia/Reoxygenation Protocol

The hypoxia/reoxygenation protocol is similar to the one described in Chapter 3. C57 mice (n=4) implanted with a dorsal window chamber were placed into a hollow acrylic restraining tube with a side slit that allowed for chamber visualization. The side of the restraining tube was connected to an outflow of pressurized air that either contained 21% O_2 or 8% O_2. The source of the air was controlled through a manual flow regulator (Cole-Palmer, Vernon Hills, IL). The mice were initially placed at

21% O_2 for 10 minutes to allow for the animal to acclimate to the tube environment. After acclimatization hypoxia was induced by flowing 8% O_2 pressurized air for 10 minutes. After hypoxia, reoxygenation was carried out for 20 minutes by flowing 21% O_2 pressurized air. After the 20 minutes, the same hypoxia/reoxygenation cycle was repeated 2 more times, for a total of 3 hypoxia/reoxygenation cycles per animal.

4.2.2 HSI Acquisition

Using the experimental setup described in Chapter 3, the automated imaging script was set to record 30 images, at 1 minute between each image, for each hypoxia/reoxygenation cycle. This resulted in one picture every minute throughout the entirety of the hypoxia/reoxygenation process. This was repeated for each hypoxia/reoxygenation cycle for a total of 90 images per animal.

After image processing following the same pipeline as described in Chapter 3 and shown in Figure 3.2, regions of interest within arterioles and venules were selected for analysis of the Hb O_2 saturation at each measured timepoint. The same arterioles and venules were selected across timepoints and hypoxia/reoxygenation cycles for any given animal. On average 2 arterioles and 2 venules were measured for each animal, and 1-2 regions within those arterioles and venules were selected for analysis. Selection of arterioles and venules was determined by their visibility and permanence within the field-of-view across all timepoints and cycles.

4.2.3 Second Order Linear System Model

A second order linear system can be described by the general second order differential Equation 4.1

$$\tau^2 \frac{d^2Y}{dt^2} + 2\zeta\tau \frac{dY}{dt} + Y = X(t) \tag{4.1}$$

where $Y(t)$ corresponds to the output variable of the system and $X(t)$ is the forcing function of the system [96]. For this specific application, the input to the system will

be the experimental changes in O_2, and the system itself would be the mouse window chamber microcirculation. For this specific model, $Y(t)$ would correspond to the hyperspectrally measured HbO_2, whereas the forcing function $X(t)$ will correspond to the changes in the external O_2 source.

The transfer function for such a system is given by Equation 4.2

$$\frac{Y(s)}{X(s)} = \frac{1}{\tau^2 s^2 + 2\tau\zeta s + 1} \tag{4.2}$$

where s is the independent variable in the Laplace domain. From this expression, it is then evident that the dynamics of the second order system are dominated by the input forcing function $X(s)$ and the constants τ and ζ, where τ corresponds to the natural period of oscillation in the absence of damping, and ζ corresponds to the damping ratio of the system.

In the proposed experimental setup, the input O_2 flow into the mouse can be considered as an on-off response. In other words once the hypoxic air flow is activated, it is assumed that all the normoxic air is immediately displaced from the environment such that the mouse is only breathing hypoxic air. The same assumption is made for the reoxygenation period, when hypoxic air is turned off and normoxic air is made available again. This assumption is expected to be valid as long as there is significant convective flow from the inflow system, which is the case for the proposed experimental preparation. Other modeling attempts for similar applications have made use of a similar assumption [97]. Given this, the input to the system $X(t)$ can be modeled as an input step response of magnitude α, such that the Laplace transform for the input yields $X(s) = \frac{\alpha}{s}$. With this, the output of our system then becomes

$$Y(s) = \frac{\alpha}{s} \frac{1}{\tau^2 s^2 + 2\tau\zeta s + 1} \tag{4.3}$$

The solution to this equation will depend on the nature of the roots in the

polynomial of the denominator. To illustrate this, Equation 4.3 can be rewritten as

$$Y(s) = \frac{\alpha}{s} \frac{1}{\left(s + \frac{\zeta}{\tau} + \frac{\sqrt{\zeta^2-1}}{\tau}\right)\left(s + \frac{\zeta}{\tau} - \frac{\sqrt{\zeta^2-1}}{\tau}\right)} \tag{4.4}$$

From this expression, three different scenarios can be derived: the case when $\zeta > 1$, or the overdamped case, the case when $\zeta = 1$, or the critically damped case, and the case when $\zeta < 1$ or the underdamped case. Study of the experimental results obtained for the HbO_2 response in arterioles and venules in the mouse window chamber after restoration of normoxic air suggests the presence of an underdamped response. This means that $\zeta < 1$ for our system, which yields the solution for Equation 4.4 to be given by

$$Y(t) = C_1 + e^{-\frac{\zeta}{\tau}t}\left(C_2 cos\sqrt{1-\zeta^2}\frac{t}{\tau} + C_3 sin\sqrt{1-\zeta^2}\frac{t}{\tau}\right) \tag{4.5}$$

where the original constant α is absorbed into the constants C_1, C_2 and C_3 [96]. With this equation available, then C_1, C_2, C_3, ζ, and τ are all parameters that were fitted through a traditional least-squares approach given $Y(t)$ and t, where $Y(t)$ corresponds to the measured Hb O_2 saturation, and t the time at which it was measured.

4.2.4 Statistical Analysis and Curve Fitting

The average value for the Hb O_2 saturation per timepoint for all arterioles, and separately, for all venules was used to generate the Hb O_2 hypoxia/reoxygenation timecourses. The reoxygenation timecourses for each of the three hypoxia/reoxygenation cycles were curve fitted to the proposed second order linear model using a least-squares approach through GraphPad Prism 7 (GraphPad, San Diego, CA). r^2 values were calculated for every fit. Due to natural variability between animals, a new set of fits were generated for each animal. Arterioles and venules also received a different

fit, resulting in a total of 6 different fits per animal. Unless otherwise noted, error bars represent the standard deviation of the measurements.

Figure 4.1: Arteriolar HbO_2 saturation timecourse during multple hypoxia/reoxygenation cycles for 4 different mice (M1-4). Yellow, blue and red lines represent cycles 1, 2 and 3 respectively. Black arrow represents timepoint at which 21% O_2 flow was restored. Error bars represent standard deviation of the HbO_2 saturation across all measured arteriolar regions of interest.

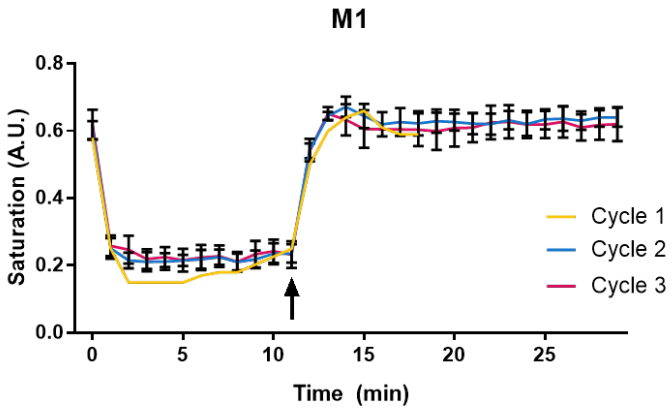
M1
Saturation (A.U.)
0.0
0.2
0.4
0.6
0.8
0
5
10
15
20
25
Time (min)
Cycle 1
Cycle 2
Cycle 3

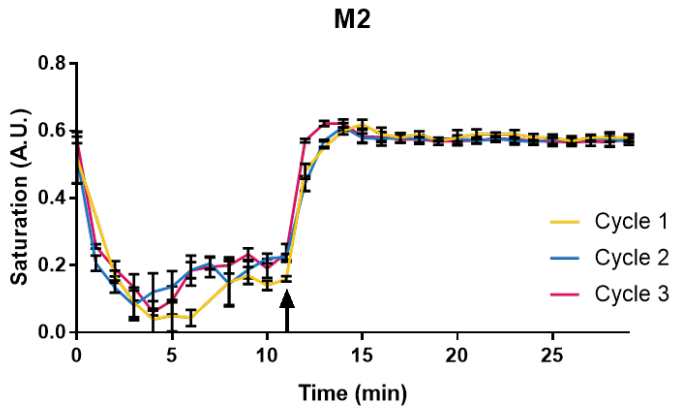
M2
Saturation (A.U.)
0.0
0.2
0.4
0.6
0.8
0
5
10
15
20
25
Time (min)
Cycle 1
Cycle 2
Cycle 3

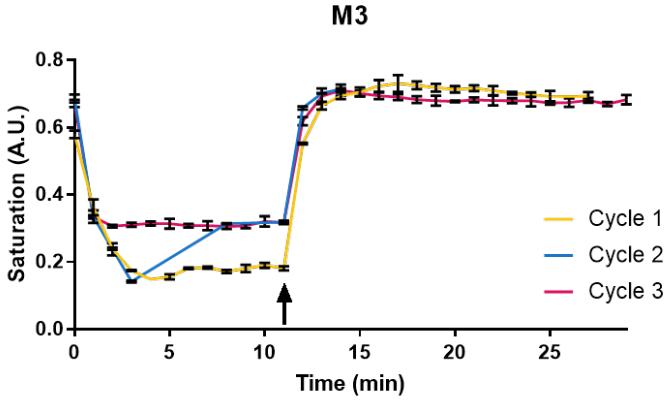
M3
Saturation (A.U.)
0.0
0.2
0.4
0.6
0.8
0
5
10
15
20
25
Time (min)
Cycle 1
Cycle 2
Cycle 3

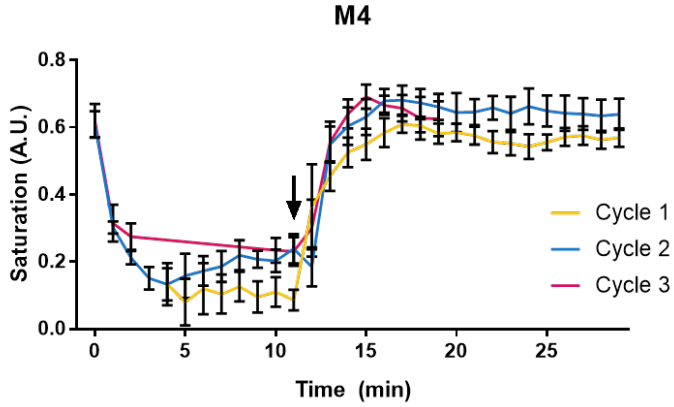
M4
Saturation (A.U.)
0.0
0.2
0.4
0.6
0.8
0
5
10
15
20
25
Time (min)
Cycle 1
Cycle 2
Cycle 3

Figure 4.2: Venular HbO_2 saturation timecourse during multple hypoxia/reoxygenation cycles for 4 different mice (M1-4). Yellow, blue and red lines represent cycles 1, 2 and 3 respectively. Black arrow represents timepoint at which 21% O_2 flow was restored. Error bars represent standard deviation of the HbO_2 saturation across all measured venular regions of interest.

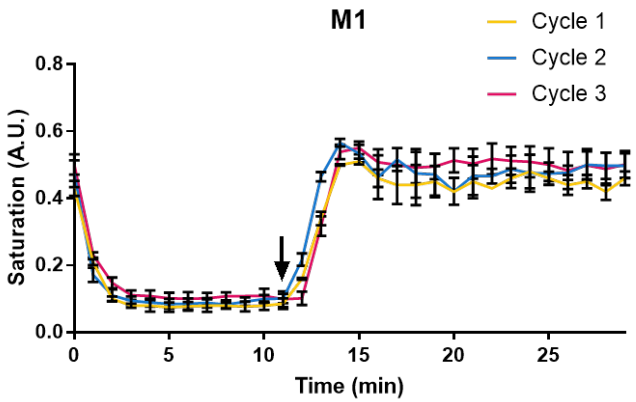
M1
Cycle 1
Cycle 2
Cycle 3
Saturation (A.U.)
0.0
0.2
0.4
0.6
0.8
0
5
10
15
20
25
Time (min)

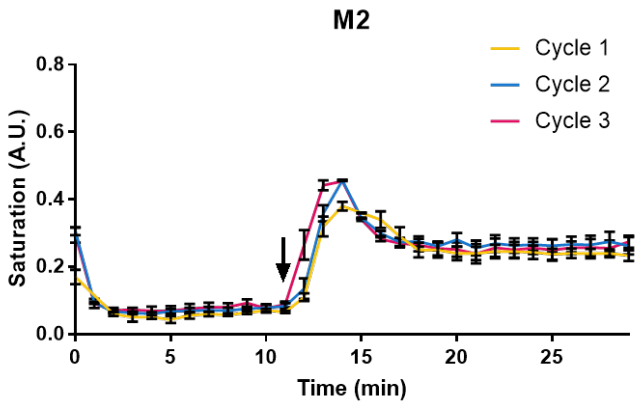
M2
Cycle 1
Cycle 2
Cycle 3
Saturation (A.U.)
0.0
0.2
0.4
0.6
0.8
0
5
10
15
20
25
Time (min)

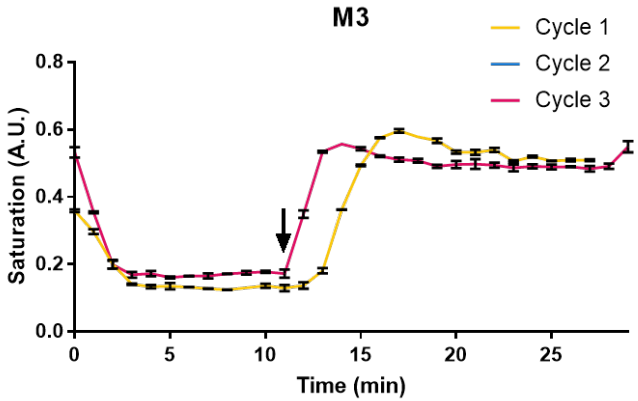
M3
Cycle 1
Cycle 2
Cycle 3
Saturation (A.U.)
0.0
0.2
0.4
0.6
0.8
0
5
10
15
20
25
Time (min)

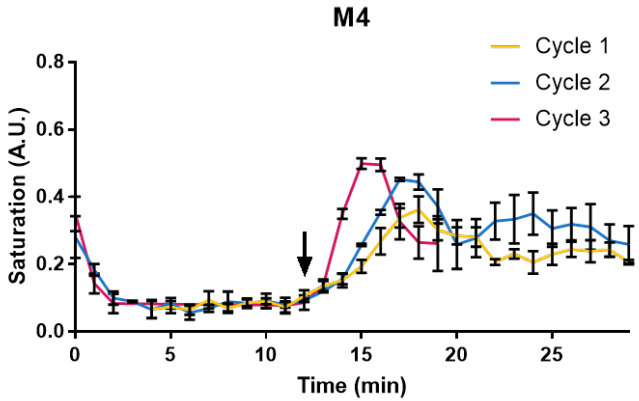
M4
Cycle 1
Cycle 2
Cycle 3
Saturation (A.U.)
0.0
0.2
0.4
0.6
0.8
0
5
10
15
20
25
Time (min)

4.3 Results

4.3.1 Hypoxia/Reoxygenation Timecourses

The corresponding timecourses for hypoxia/reoxygentaion for each animal are shown in Figures 4.1-4.2. Each cycle is plotted on the same graph for each animal M1-4. Hypoxia is started right after the first datapoint at $t = 0$ and reoxygenation after the black arrow at $t = 11$. The error bars represent the standard deviations for the saturation measurements at multiple regions-of-interest within the timepoint, therefore they represent the regional variations in saturation within the microcirculation.

A seemingly apparent trend in Figure 4.1 is that after subsequent hypoxia cycles, the arteriole saturation during hypoxia seems to reach different stable values. It appears that subsequent hypoxia cycles lead to an increase in the arteriole saturation level that is achieved during the hypoxic period. During recovery, however, it seems that regardless of the hypoxic cycle, the final arteriole saturation reaches a very similar endpoint. There are also different dynamic responses during reoxygenation which will be characterized by the proposed model.

In Figure 4.2 the behavior during hypoxia is similar that to that seen in the arterioles, in that subsequent hypoxic cycles lead to a higher saturation during hypoxic period. This effect, however, is present to a lesser extent than in the arterioles. During the reoxygenation, it can be seen that different cycles have different dynamic responses, which will be characterized by the proposed model.

4.3.2 Model Fitting

The resulting fits for the reoxygenation timecourse for a representative animal (M2) are shown in Figure 4.3. The x-axis was rescaled to start from zero. Also note the differences between the y-axis. For the venules, the fits were started one timepoint

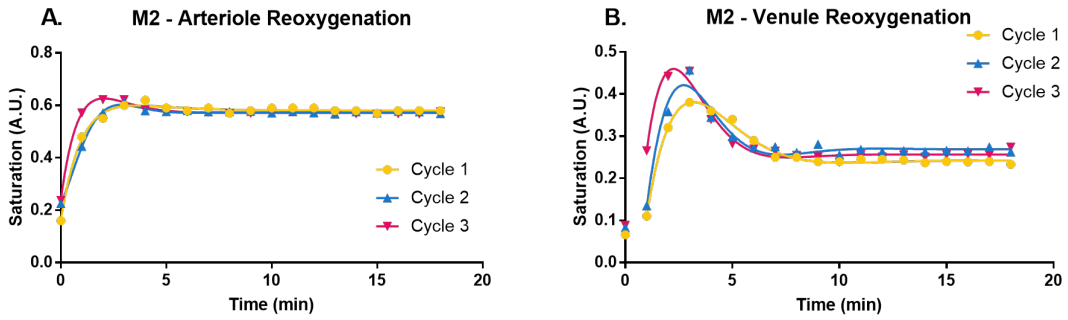

Figure 4.3: Reoxygenation timecourse and corresponding fit to the proposed second order linear system model for **A.** arterioles and **B.** venules in a representative mouse (M2). The arteriolar fits in **A.** had r^2 values 0.991, 0.997 and 0.997; ζ values 0.99, 0.64 and 0.89; and τ values 1.37, 0.80 and 1.00, for cycles 1, 2 and 3 respectively. The venular fits in **B.** had r^2 values 0.947, 0.946 and 0.970; ζ values 0.74, 0.62 and 0.73; and τ values 1.53, 1.14 and 1.16, for cycles 1, 2 and 3 respectively.

after the cessation of hypoxia ($t = 12$ in Figure 4.2, or $t = 1$ in Figure 4.3B). This was done due to a characteristic delay in the recovery of the venular saturation, which was also observed in the hamster window chamber model as shown in the results section of Chapter 3. This delay in the recovery can be accounted for with the proposed second order model, but it significantly affects the damping coefficient and natural period of the fitted model. Since the emphasis of this work is in modeling the compensatory response during reoxygenation, the effect of this initial delay ought to be neglected to ensure accurate modeling of the remainder of the response.

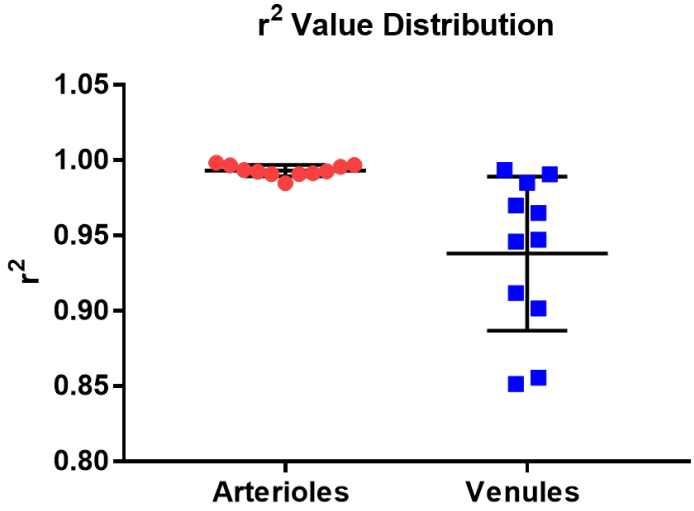

Figure 4.4: Distribution of r^2 goodness-of-fit values for all fits performed in arterioles and venules across all animals and cycles. Mean r^2 value for arterioles was 0.993 and for venules 0.938.

The distribution of r^2 values in all the model fits done for arterioles and venules across all animals and cycles is shown in Figure 4.4. The distribution of values for the arteriole fits is very tight, and centered around a mean r^2 of 0.993. The distribution of values of the venule fits is wider, and it is centered around a mean r^2 of 0.938. They both, however, suggest a strong correspondance between the mathematical model and the observed experimental data, confirming the validity of the model.

4.3.3 Dynamic Response During Reoxygenation

The dynamics of the proposed second order model can be characterized by the damping ratio ζ and the natural period τ. These two parameters are directly obtained from the corresponding fits and are shown in Figure 4.5 for arterioles, venules and each cycle. The values correspond to the average across all animals,

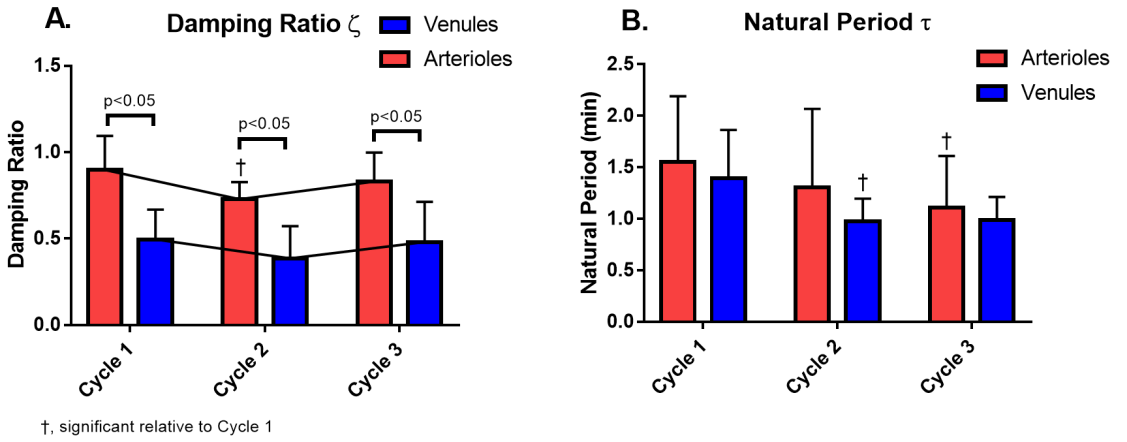

Figure 4.5: **A.** Damping ratio and **B.** natural period of the reoxygenation HbO_2 saturation response in arterioles and venules. The values include the average across all animals for a given cycle, and error bars represent the standard deviation of the value. The † corresponds to a statistically significant difference relative to the value at Cycle 1.

with the error bars representing the standard deviation.

The resulting damping ratios are shown in Figure 4.5A. Statistically significant differences between arterioles and venules were found in all cycles. For arterioles, there is a statistically significant decrease in the second cycle relative to the first. No statistically significant differences were found between the third cycle and the first or second cycle, although there appears to be a non-statistically significant increase in the damping ratio between the second and third cycle. In the venules, no statistically significant changes in the damping ratio were found across cycles, however, the same trend as the one found in the arterioles seems to be present, but to a lesser extent.

The resulting natural periods are shown in Figure 4.5B. No statistically significant differences were found between arterioles and venules in any of the cycles. It seems, however, that the natural period for the venular recovery is slightly below that of the arterioles in every case. For the arterioles, it seems that subsequent cycles decrease the natural period of the reoxygenation response. While natural period

being lower after every cycle, there are no statistically significant differences between cycle 1 and cycle 2, or cycle 2 and cycle 3. The natural period at cycle 3, however, is statistically lower that at cycle 1. In the venules a similar trend is observed, where the natural period at cycle 1 is larger than at cycles 2 and 3. For the venules, however, cycle 2 is significantly lower than cycle 1, with no significant differences between any other cycles. Correct intepretation of these results must take into account that the response for the venules was modeled starting 1 minute after the response of the arterioles due to the known delay between the two responses.

4.4 Discussion

The results presented in this study show that the dynamics of the recovery of hemoglobin oxygen saturation in the microcirculation after hypoxic insult can be measured through HSI approaches, and accurately modeled by a second order linear system. The resulting goodness-of-fit as estimated by the r^2 values shown in Figure 4.4 suggest that the proposed model is an accurate representation of the behavior of the dynamics of the system.

The reoxygenation overshoot in response to hypoxia cessation modeled in this study has not been carefully studied before in the microcirculation. In the case of tissue pO_2, this behavior has been observed in brain tissue and isolated hippocampal slices [98, 99]. Similar measurements and HbO_2 saturation responses as the ones described in this study have been shown by Hashimoto et. al. [100], but very little emphasis was placed in modeling, understanding and describing the observed dynamics, even though measurements were done in both vanuels and arterioles. A very similar circulatory response, however, has been investigated extensively, and that is post-occlusive reactive hyperemia. Post-occlusive reactive hyperemia is a period of increased bloodflow (i.e. an overshoot) prior to the flow returning to baseline levels resulting from termination of an occlusion in a blood vessel [101]. This behavior has

been extensively studied in the brain [102] and in the skin [103], the latter being particularly relevant for clinical purposes. The magnitude of the bloodflow overshoot as well as the timecourse of the response have been related to skin microvascular function, as well as the general state of the microcirculation across the body [104, 105]. Studies have shown that this increase in bloodflow is associated to the vasodilation resulting from the ischemic period [101]. Another consequence of the increase in flow is that it often results in an increase in the "tissue saturation", as shown by [103], which implies an increase in the amount of HbO_2 saturation arriving to the tissues during this overshoot period. Many of the HbO_2 saturation measurements carried out in the study of reactive hyperemia have been done by means of transdermal near-infrared spectroscopy (NIRS), which measures the volume average saturation in the measured region [106, 103, 105]. This is a limitation, as it severely limits the spatial resolution of the measurement, not allowing to understand if the response is dominated by the behavior of the venules and arterioles. Other techniques based on photoacoustic imaging of the cutaneous microcirculation have attempted to solve this problem [107], as well as previous studies in animal models [108, 109]. Due to the clinical relevance of this response, several groups have attempted to develop mathematical models that allow to describe the dynamics, and have found that differences in the parameters of the model correlate with certain pathological conditions [101, 107].

Many of the mechanisms involved in post-occlusive reactive hyperemia are likely to be present in the post-hypoxic reoxygenation response that has been presented in this study. However, there are some key differences between the post-occlusive response and the hypoxic response that have been portrayed in the literature. Both phenomena are a response to a decreased amount of oxygen arriving to the microcirculation, but the origin of the decrease in oxygen availability is very different in both cases. For the post-occlusive case, there is a physical occlusion in the bloodflow, suggesting a decreased amount of blood arriving to the microcircula-

tion. In the hypoxic case, there is no occlusion, so the amount of blood flowing to the microcirculation is unhindered by the insult. In fact, it has been shown that microvascular blood velocity is increased during the hypoxic period in both animal and human studies in the skin and brain microvasculature [110, 111, 112, 97, 113, 114]. This is different from the occlusion case where the flow is known to decrease during the ischemic period. Skin microvascular perfusion studies, following a similar acute hypoxia/reoxygenation protocol as the one described in this study, show that the bloodflow in the skin microcirculation does remain elevated after termination of the hypoxic insult, which can lead to a similar behavior to the one resulting from post-occlusive reactive hyperemia [111, 110]. However, results from those studies do not suggest the presence of a inherent microvascular endothelial response as the consequence for this increased bloodflow in the post-hypoxic reoxygenation period. This suggests a key difference between the post-occlusive reactive hyperemia response, and the post-hypoxia reoxygenation response observed in this study, emphasizing the importance of the modeling described in this study.

The proposed second order linear system model of reoxygenation oxygen dynamics is consistent with the hyperspectrally measured HbO_2 saturation as suggested by the obtained r^2 values (Figure 4.4). The ability to characterize the response of the system through the damping ratio and the natural period allows for a quantitative way to determine the post-hypoxia reoxygenation HbO_2 response. The natural period, which is equivalent to the inverse of the natural frequency of the response allows to describe how fast the system responds to the input change. Since the input change for the proposed system is a step response in the inspired oxygen by the animal, the natural period characterizes how fast the Hb O_2 saturation adapts in reponse to that step change. In both arterioles and venules, in general, the natural period of the Hb O_2 saturation recovery decreases with subsequent hypoxic cycles. A decrease in the natural period is equivalent to an increase in the natural frequency, which signifies a faster recovery of the Hb O_2 saturation. The fact that this natural

frequency increases over time might imply that after subsequent hypoxic insults, the animal adapts and is capable of responding much quicker when the oxygen becomes available once again. To our knowledge, this is the first time such behavior has been modeled. Furthermore, making the distinction between the response in the arterioles and venules is novel, as this is not achievable through non-invasive approaches such as NIRS.

The damping ratio also portrays interesting dynamics of the system. The damping ratio is a good quantification of the amount of overshoot of the system, which can be described by Equation 4.6

$$Overshoot = exp\left(\frac{-\pi\zeta}{\sqrt{1-\zeta^2}}\right) \tag{4.6}$$

where ζ corresponds to the damping ratio of the system. Therefore, for decreased damping ratios, the larger the overshoot of the system [96]. Similarly the decay ratio of the system is given by $overshoot^2$. The decay ratio characterizes how fast the response of the system reaches a stable value, therefore, for decreased damping ratio, the longer the time it takes for the system to reach its stable value. With this in mind, the resulting damping ratios for the post-hypoxic reoxygenation response suggest key differences in the response of HbO_2 saturation in arterioles and venules to the hypoxic insult. The damping ratio of arterioles was significantly higher than the one of the venules for all cycles. This suggests that the stabilization of the HbO_2 saturation in arterioles happens significantly faster than in venules. It is important to understand that the dampening of the response is independent to the response time described by the natural period τ, which is very similar for arterioles and venules. In fact, even with the 1 minute offset of the venular response with respect to the arteriolar response, if the hemodynamic effects were the dominant factor for the dynamics, the response after that 1min offset should be very similar since the natural periods are very similar. Furthermore, it is known that hemodynamic effects such flow changes are dominant in the arteriolar side and not in the venular side,

since the arterioles have higher upstream pressures and are more directly regulated by changes in cardiovascular function than venules. This suggests any changes due to hemodynamic effects would be predominantly observed in the arterioles, and that the slightly underdamped response observed in these arterioles can be attributed, to some extent, to hemodynamic effects. Furthremore, the decrease in the damping ratio after the initial hypoxia/reoxygenation cycle might be evidence of a more extreme cardiovascular (i.e. higher heart rate and/or blood pressure) response after the initial cycle, replicated in the arterioles. But the same argument does not hold for venules, therefore differences between the arteriolar and venular damping must involve tissue oxygen consumption mechanisms.

The decreased damping ratio of the arterioles suggests a fast stabilization of the HbO_2 saturation in these vessels. This means, that the oxygen supply for the tissues and the venules is rapidly reestablished and constant. Furthermore, since the venular response is offset by approximately 1 minute, the overshoot phase of the arterioles will have mostly terminated and the HbO_2 saturation will have stabilized by the time the venular overshoot phase is developing. This is important because it implies that the dynamics observed in the venules is not dictated by the arteriolar dynamics, but instead, they must be influenced by the behavior of the tissue. Studies that do not involve hemodynamic effects, such as brain slice oxygen measurements after hypoxic insult have shown overshoot behaviors very similar to the ones observed in the venules in this study [99]. While the studies involving brain slice pO_2 measurements attribute a great portion of the overshoot to the measurement of a transient increase in free radicals after the hypoxic period, another part of the overshoot is attributed to a transient decrease in oxygen consumption during the hypoxia and shortly after the oxygen is restored. Since the approach used in this study only responds to changes in HbO_2 saturation, the increased measured venular oxygenation cannot be attributed to increased free radicals, but it can be attributed to decreased oxygen consumption by the tissue, which is consistent with the obser-

vations in [99]. Studies in cell cultures have also suggested that the presence of acute hypoxia decreases oxygen consumption in certain cell types [115]. Acute hypoxia has also been shown to cause increased superoxide formation during the hypoxic period, likely leading to subsequent regulation of oxygen consumption and promotion of HIF transcription for long term chronic hypoxia adaptation [116, 117, 118]. While many of these metabolic changes take place during the hypoxic period, they will likely require some time in order to revert once the hypoxia has ceased. This evidence points towards decreased tissue oxygen consumption during the initial stages of reoxygenation as the main culprit for the observed venular overshoot. If the tissue consumption is decreased during hypoxia and shortly after reoxygenation, then the amount of oxygenated blood that arrives from the arterioles to the venules will be larger than when the tissue restores its baseline oxygen consumption, providing an explanation for the observed overshoot. The slight decrease in the dampness of the system after the initial hypoxia/reoxygenation cycle might indicate that repeated hypoxia reoxygenation cycles lead to the accumulation of free radicals and transcription factors, which further inhibit the oxygen consumption in the presence of subsequent hypoxic insults.

Much like how the modeling of post-occlusive reactive hyperemia provides insights into different pathologies [101], the modeling of this post-hypoxic reoxygenation response can be valuable for characterizing the effects of hypoxia in different pathologies. As mentioned, acute hypoxia is known to cause increases in the production of free radicals by cells [118], therfore subsequent exposures to hypoxia, such as during sleep apnea, are likely to cause progressive accumulations of these free radicals over time. It is possible that by characterizing the overshoot of the venular HbO_2 saturation reoxygenation response after the hypoxia/reoxygenation cycles, as done in this study, important insights regarding the formation of free radicals during sleep apnea can be uncovered. Furthremore, the use of this modeling approach in predominantly hypoxic tissue enviornments, such as malignant tumors, might al-

low to characterize how different types of cancer respond to hypoxia/reoxygenation, and the effects altitude changes, sleep apnea, and other conditions can have on the progression and metastasis of the disease.

The largest limitation of this study is that no other hemodynamic parameters were measured in conjunction with the HbO_2 saturation during the hypoxia/reoxygenation cycles. Future studies will aim to measure vessel diameter as well as bloodflow using a similar experimental procedure in an attempt to further understand the underlying mechanisms that dictate the modeled dynamics. Disease models, such as sickle cell and thalacemia will also be studied to assess how the model parameters change in the presence of pathophysiological conditions.

4.5 Conclusions

The results presented in this study show that the dynamics of the recovery of HbO_2 saturation in the microcirculation after hypoxic insult can be measured through HSI approaches, and accurately modeled by a second order linear system. Careful understanding and modeling of these reoxygenation dynamics, as shown in this study, can aid in better understanding the response of the microcirculation to hypoxic insult. Future studies should focus in applying similar models for the reoxygenation dynamics under pathophysiological conditions, such as sleep apnea or sickle cell disease, in an attempt to better quantify the microcirculatory response, and acquire more quantitative methods for assessing the severity of these conditions under hypoxia.

Chapter 5

Use of Hyperspectral Imaging for Determining Intravascular Changes in Oxygen Saturation During Hemorrhagic Shock in a Hamster Window Chamber Model

The previous two chapters focused on the use of HSI for the study of hypoxia in the microcirculation, specifically hypoxia induced by decreased environmental oxygen availability. This chapter will focus in studying the oxygenation state of the microcirculation in the presence of a different type of hypoxia, namely the one caused by the decreased amount of oxygen carrying red blood cells (RBCs). This chapter will illustrate the important differences between arteriole and venular hemoglobin oxygen saturation during onset and recovery from hemorrhagic shock, as measured using the developed hyperspectral imaging approach. This chapter will be signficantly shorter than the last two as it is currently work in progress, but will present some preliminary

results that validate the use of HSI for the monitoring of hemorrhagic shock.

5.1 Introduction

Hemorrhagic shock (HS) is a form of hypovolemic shock resulting from severe blood loss [119]. HS deaths account for around 60000 of the deaths in the United States, and the survivors often have poor outcomes and increased chance of long-term mortality [119, 120]. The negative prognosis associated with HS is a consequence of the widespread physiological effects shock has on the body. The liver [121], kidneys [122], and the heart [123], are all severely affected after the onset of HS, and the duration of the insult will be proportional to the severity of the tissue damage associated with it.

In the presence of a severe hemorrhage in a clinical setting often involves the activation of a massive transfussion protocol (MTP), which involves the transfusion of up to 10 units of packed red blood cells (pRBC) in a period of 6 hours. In many of these instances, however, it is hard to determine a clear endpoint for the resuscitation [124]. Point-of-care assessments such as thromboelastography, are often used when available. However, field and community hospitals do not have access to these technologies and often times must resort to a goal blood pressure guided approach, such as maintaining MAP above $90 mmHg$. Other guidelines suggest the monitoring of other parameters such as oxygen saturation, lactate base deficit, heart rate, and mixed central venous oxygen saturation [125]. However, a comprehensive understanding on how changes in these parameters actually reflect changes in the microcirculatory organ perfusion is lacking.

In the literature of blood substitutes and reperfusion fluids, a hemodynamic argument for the recovery from shock is often presented. Functional Capillary Density (FCD) has been used extensively for measuring the recovery of tissue perfusion [126, 127, 128], and has been positively associated with the recovery from hemor-

rhagic shock. The other line of thought suggests that simply restoring MAP and FCD is not sufficient to accurately restore oxygen carrying capacity in the microcirculation beds of different tissues, and is supported by experimental evidence [129, 130]. The argument follows that even though gross systemic hypotension is corrected, as suggested by the restoration of MAP and FCD, there is still an inadequate oxygen distribution, which can result in isolated organ ischemia, and then subsequent whole-body ischemia [130]. A more careful understanding of the oxygenation state of the microcirculation during and after HS resuscitation might help elucidate these arguments.

This study uses hyperspectral imaging (HSI) for the study of the changes in arteriolar and venular HbO_2 saturation in a hamster window chamber model during HS and resuscitation with Hextend, a plasma volume expander, and blood. Parameters commonly associated with recovery from hemorrhagic shock including MAP, heart rate and lactate were also measured and compared between groups.

5.2 Methods

The HSI system, the HSI processing pipeline and the animal preparations are identical to those described in Chapter 3. Please refer to the corresponding sections in that chapter for more details.

5.2.1 Hemorrhagic Shock Protocol

Animals were hemorrhaged by an amount equivalent to 50% of their blood volume over 10 minutes by drawing blood from the arterial catheter. The shock was sustained for 5 minutes. The animal was subsequently resuscitated during 10 minutes with an amount equivalent to 25% of its original blood volume using either Hextend (n=2) or the animal's own blood (n=2), infused through the arterial catheter. After resuscitation, the animal was observed for 1 hour during recovery.

5.2.2 HSI Acquisition

Using the experimental setup described in Chapter 3, the automated imaging script was set to record 10 images, at 1 minute per image during the hemorrhage period; 2 images, at 2.5 minutes per image, during the shock period; 10 images, at 1 minute per image during the resuscitation period; and 12 images, at 5 minutes per image, during the recovery period. This resulted in a total of 34 images per animal.

After image processing following the same pipeline as described in Chapter 3 and shown in Figure 3.2, regions of interest within arterioles and venules were selected for analysis of the Hb O_2 saturation at each measured timepoint. The same arterioles and venules were selected across timepoints and hypoxia/reoxygenation cycles for any given animal. On average 2 arterioles and 2 venules were measured for each animal, and 1-2 regions within those arterioles and venules were selected for analysis. Selection of arterioles and venules was determined by their visibility and permanence within the field-of-view across all timepoints and cycles.

5.2.3 Systemic Parameters

For MAP and HR measurements, the arterial line was connceted to a pressure transducer connected to a digital acquisition system (MP150, Biopac Systems, Goleta, CA). MAP and HR were measured at baseline, during shock, and every 10 minutes during the recovery period.

5.2.4 Arterial Lactate and Saturation

Arterial lactate and saturation were measured from arterial blood samples measured using an ABL 90 blood gas analyzer (Radiometer, Denmark) at baseline, at the end of shock and at the end of the experiment to minimize the amount of blood removed.

5.2.5 Results

5.2.6 Microvascular HbO_2 Saturation Timecourse

The HbO_2 saturation measured during hemorrhage, shock, resuscitation and recovery, relative to baseline, is shown in Figure 5.1. Each line corresponds to the average value of the saturation for that specific experimental group and vessel across two different animals. Error bars are omitted for clarity, but there was significant variation between animals during hemorrhage, shock, and infusion, with more consisten values during the recovery period. During the resuscitation period, the HbO_2 saturation in the arterioles of both the Hextend and the blood groups recovered in a similar fashion, with the ones for the blood group recovering slightly faster. Only the venular HbO_2 saturation for the blood group recovered during the infusion period. During the recovery period, the arteriolar HbO_2 saturation for both groups remained relatively constant and close to the original baseline value, with the value for the blood group being slightly above the value for the Hextend group. The venular HbO_2 saturation, on the other hand, behaved very different for both groups during the recovery period. For the blood group, the venular HbO_2 saturation recovered to slightly above its baseline value initially, and then subsequently oscillated around $\pm 10\%$ of its baseline value. For the Hextend group, however, the venular HbO_2 saturation did not recover to more than 50% of its baseline value during the recovery period, or at any point during the experimental procedure.

5.2.7 MAP Timecourse

The MAP timecourse measured at baseline, beginning and end of shock, and during resuscitation is shown in Figure 5.2. It can be seen that both experimental groups behaved similarly during hemorrhage, shock, and resuscitation. During recovery, there were more pronounced differences between the blood and Hextend groups,

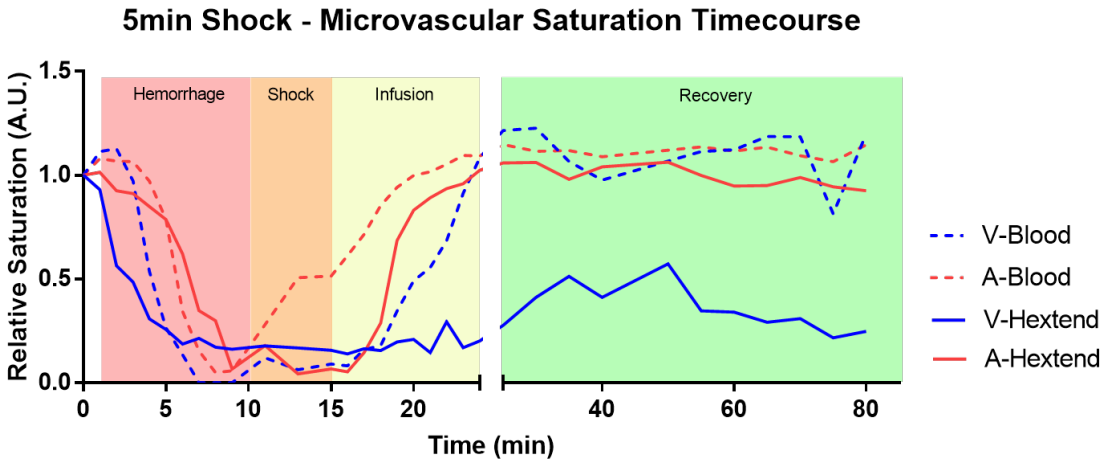

Figure 5.1: HbO_2 saturation timecourse for arterioles (red) and venules (blue) for the blood (dashed lines) and Hextend (full lines) experimental groups. Data is shown relative to baseline values. Data is shown in 1min intervals for hemorrhage, shock and resuscitation/infusion timepoints, and in 5min intervals for the recovery timepoints.

with the Hextend group having an average MAP of $80.0mmHg$ and the blood group an average MAP of $112.4mmHg$. The HR (not shown) shows significant variability during the hemorrhage, shock and resuscitation period, between animals and between groups. During the recovery period, the average HR for the Hextend group was $458.8bpm$ and $444.8bpm$ for the blood group.

5.2.8 Arterial Lactate and Saturation

The lactate and arterial saturation as measured by arterial blood samples are shown in Figure 5.3. It can be seen that both experimental groups have similar lactate values at all measured timepoints. The arterial saturation in the Hextend group appears to be elevated by about 8% relative to the blood group. The small sample size of this study does not allow to determine statistically significant differences between groups.

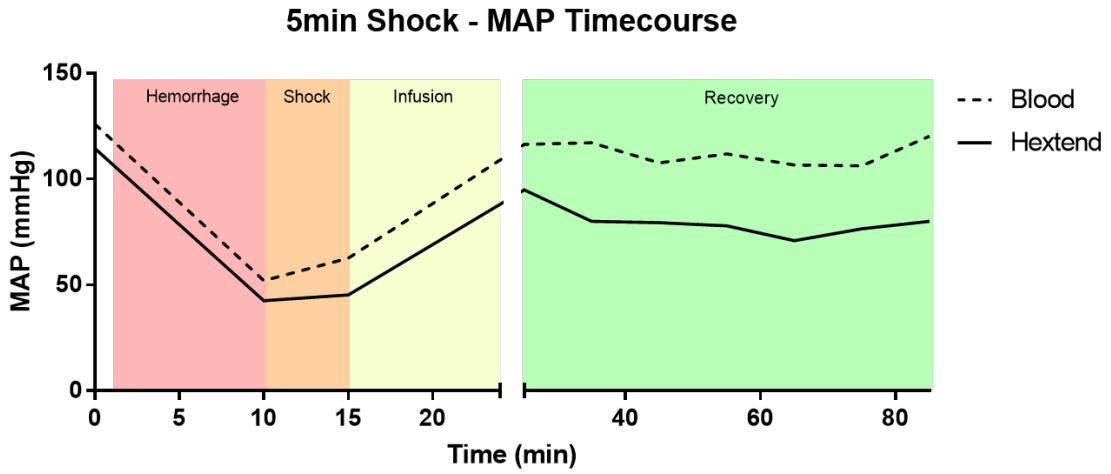

Figure 5.2: MAP timecourse for the blood (dashed lines) and Hextend (full lines) experimental groups.

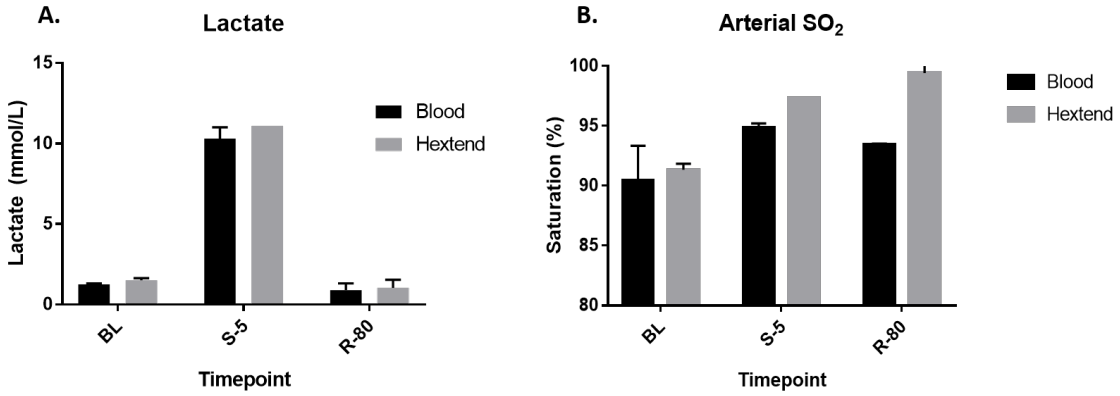

Figure 5.3: **A.** Systemic lactate and **B.** arterial oxygen saturation as measured by blood gas analysis of arterial samples. Timepoints represent baseline (BL), end of shock (SH-5), and end of recovery (R-80).

5.3 Discussion

The main finding of this preliminary study is that HSI can be used to find marked differences between the microcirculatory HbO_2 saturation in arterioles and venules, during and after HS, and in the presence of different resuscitation fluids. While hyperspectral imaging has been used for the study of HS [27], it has only been done either transdermally or at the surface of internal organs, which provides and average metric of the oxygenation state of the tissues, but not detailed information about the behavior of venules and arterioles.

The results from this study suggest that while the HbO_2 saturation in arterioles behaves very similar when resuscitating with Hextend or blood, the venular saturation behaves very differently. It can be argued that the recovery of the arteriole saturation is consistent with the hemodynamic argument. The ability of the arterioles to recovery their HbO_2 saturation using Hextend as the resuscitation fluid suggests that despite not necessarily restoring the amount of O_2 binding sites to baseline levels, the increased hemodynamic effects such as increased blood pressure and blood flow, can restore arteriolar saturation. Since oxygen exchange takes place, to an extent, in the arterioles, [43], the restoration of the saturation might imply a restoration of the ability of blood to supply oxygen to the tissue. The satisfaction of the tissue oxygen metabolic demands is observed with the recovery of the lactate values in the Hextend group.

The lack of recovery of the venular saturation in the Hextend group is an interesting finding. While the systemic lactate levels suggest that the satisfaction of the oxygen metabolic demand was equivalent in both groups, the significantly decreased venular HbO_2 recovery in the Hextend group presents contrarian evidence. A plausible explanation can be constructed using the argument of a tissue oxygen pool. In a physiologically normal state, the tissue receives a constant supply of oxygen from the arterioles, only uses what is necessary, and the remaining oxygen

continues through the microcirculation into the venules, showing the arteriolar and venular HbO_2 saturation observed at baseline. In the presence of HS, the ability of blood to carry oxygen is severely decreased, therefore the small amount of O_2 arriving from the arterioles will be consumed by the tissue, resulting in a decreased venular saturation during shock. During resuscitation with Hextend, the improved hemodynamics leads to an increased oxygen delivery to the tissues, which might allow to satisfy the minimal metabolic demand of the tissue, as suggested by the low end-resuscitation lactate levels. However, since the oxygen supply is just sufficient to satisfy the tissue oxygen supply, the amount of oxygen that continues into the venules is minimal, resulting in the decreased venular HbO_2 saturation observed for the Hextend group. For the blood group, since both the hemodynamic effects and the oxygen carrying capacity of the microcirculation are restored, the metabolic demand is satisfied, and the excess oxygen is then allowed to continue into the venular microcirculation, resulting in the close to baseline venular HbO_2 saturation observed during the recovery period.

These results show the interplay between the hemodynamic and oxygen debt arguments that dominate the HS resuscitation literature. Clinically, they also suggest that measurements of lactate, MAP, and arterial saturation as measured through pulse oximetry might be misleading indicators of complete recovery from shock. The shock done in this study was very short compared to what is usually found in the literature and in clinical settings. Yet, while MAP, HR, lactate and arterial saturation had suggested a recovery by standard means for both groups, there were significant changes in the microcirculation. The consequences of the discrepancies between the venular HbO_2 saturation recovery of the two experimental groups have to be studied further in order to arrive to better conclusions. It is likely, however, that subsequent insults such hypoxia, or even maybe physical excrusiation, might lead to a dis-compensatory response in the presence of a HS resuscitation that restores hemodynamics but not oxygen carrying capacity.

5.4 Conclusion

The results from this study show that HSI can be used for the microvascular monitoring of HS in a hamster window chamber model. The HbO_2 saturation differences found between venules and arterioles in the presence of a plasma expander, and blood, used as resuscitation fluids, showed important differences between the two resuscitation approaches that must be studied further.

Chapter 6

Conclusion

The work presented in this thesis has served to illustrate the applicability of hyperspectral imaging for the study of the hemoglobin oxygen saturation dynamics in the microcirculation. Previous works in the literature have focused in using a very constrained set of hyperspectral imaging techniques for *in vivo* microcirculation studies, but this work is aimed at extending this literature in new directions. The results from the experiments presented in this thesis demonstrate the value in using hyperspectral imaging systems with superior spatial resolution, such as spatial-scanning systems. Furthermore, while the use of hyperspectral imaging *in vivo* has been very application oriented, with emphasis on applications for the study of tumor and brain microvasculature, this work suggests that fundamental principles of the microcirculation, previously unveiled by older techniques, can, and should, now be reassessed using this technology.

This thesis, in full, is currently being prepared for submission for publication of the material. Lucas, Alfredo; Munoz, Carlos; Cabrales, Pedro. The thesis author was the primary author of this material.

Bibliography

[1] A. F. H. Goetz, "Three decades of hyperspectral remote sensing of the Earth: A personal view," *Remote Sensing of Environment*, vol. 113, pp. S5–S16, Sept. 2009.

[2] M. Kubik, "Chapter 5 Hyperspectral Imaging: A New Technique for the Non-Invasive Study of Artworks," in *Physical Techniques in the Study of Art, Archaeology and Cultural Heritage* (D. Creagh and D. Bradley, eds.), vol. 2 of *Physical Techniques in the study of Art, Archaeology and Cultural Heritage*, pp. 199–259, Elsevier, Jan. 2007.

[3] R. Siche, R. Vejarano, V. Aredo, L. Velasquez, E. Saldaa, and R. Quevedo, "Evaluation of Food Quality and Safety with Hyperspectral Imaging (HSI)," *Food Engineering Reviews*, vol. 8, pp. 306–322, Sept. 2016.

[4] G. Edelman, T. G. van Leeuwen, and M. C. G. Aalders, "Hyperspectral imaging for the age estimation of blood stains at the crime scene," *Forensic Science International*, vol. 223, pp. 72–77, Nov. 2012.

[5] M. J. Khan, H. S. Khan, A. Yousaf, K. Khurshid, and A. Abbas, "Modern Trends in Hyperspectral Image Analysis: A Review," *IEEE Access*, vol. 6, pp. 14118–14129, 2018.

[6] G. Lu and B. Fei, "Medical hyperspectral imaging: a review," *Journal of Biomedical Optics*, vol. 19, p. 010901, Jan. 2014.

[7] L. Gao and R. T. Smith, "Optical hyperspectral imaging in microscopy and spectroscopy a review of data acquisition," *Journal of biophotonics*, vol. 8, pp. 441–456, June 2015.

[8] G. Daeschlein, I. Langner, T. Wild, S. von Podewils, C. Sicher, T. Kiefer, and M. Jnger, "Hyperspectral imaging as a novel diagnostic tool in microcirculation of wounds," *Clinical Hemorheology and Microcirculation*, vol. 67, no. 3-4, pp. 467–474, 2017.

[9] W. R. Johnson, D. W. Wilson, W. Fink, M. S. Humayun, and G. H. Bearman, "Snapshot hyperspectral imaging in ophthalmology," *Journal of Biomedical Optics*, vol. 12, p. 014036, Jan. 2007.

[10] J. S. Harvey, C. R. Siviour, and H. E. Smithson, "From Spectra to Perceptual Color: Visualization Tools for the Dimensional Reduction Achieved by the Human Color Sense," 2018.

[11] Q. Li, X. He, Y. Wang, H. Liu, D. Xu, and F. Guo, "Review of spectral imaging technology in biomedical engineering: achievements and challenges," *Journal of Biomedical Optics*, vol. 18, p. 100901, Oct. 2013.

[12] P. R. Silverglate, K.-L. Shu, D. Preston, J. T. Stein, and F. R. Sileo, "Concepts for spaceborne hyperspectral imagery using prism spectrometers," in *Advanced Microdevices and Space Science Sensors*, vol. 2267, pp. 112–120, International Society for Optics and Photonics, Sept. 1994.

[13] N. Hagen and T. S. Tkaczyk, "Compound prism design principles, I," *Applied optics*, vol. 50, pp. 4998–5011, Sept. 2011.

[14] T. N. Woods, R. T. Wrigley, G. J. Rottman, and R. E. Haring, "Scattered-light properties of diffraction gratings," *Applied Optics*, vol. 33, pp. 4273–4285, July 1994.

[15] T. Vaarala, M. Aikio, and H. Keraenen, "Advanced prism-grating-prism imaging spectrograph in online industrial applications," in *New Image Processing Techniques and Applications: Algorithms, Methods, and Components II*, vol. 3101, pp. 322–330, International Society for Optics and Photonics, Aug. 1997.

[16] J. M. Eichenholz, N. Barnett, and D. Fish, "Sequential Filter Wheel Multispectral Imaging Systems," in *Imaging and Applied Optics Congress (2010), paper ATuB2*, p. ATuB2, Optical Society of America, June 2010.

[17] R. Abdlaty, S. Sahli, J. Hayward, and Q. Fang, "Hyperspectral imaging: comparison of acousto-optic and liquid crystal tunable filters," in *Medical Imaging*

2018: Physics of Medical Imaging, vol. 10573, p. 105732P, International Society for Optics and Photonics, Mar. 2018.

[18] N. Gat, "Imaging spectroscopy using tunable filters: a review," in *Wavelet Applications VII*, vol. 4056, pp. 50–64, International Society for Optics and Photonics, Apr. 2000.

[19] P. Kaur and S. Kaur, "Acousto Optic Tunable Filters," vol. 6, no. 3, p. 4, 2015.

[20] Y. Wang, N. P. Reder, S. Kang, A. Glaser, and J. Liu, "Multiplexed Optical Imaging of Tumor-Directed Nanoparticles: A Review of Imaging Systems and Approaches," *Nanotheranostics*, vol. 1, pp. 369–388, Aug. 2017.

[21] M. A. Afromowitz, J. B. Callis, D. M. Heimbach, L. A. DeSoto, and M. K. Norton, "Multispectral imaging of burn wounds: a new clinical instrument for evaluating burn depth," *IEEE Transactions on Biomedical Engineering*, vol. 35, pp. 842–850, Oct. 1988.

[22] S. V. Panasyuk, S. Yang, D. V. Faller, D. Ngo, R. A. Lew, J. E. Freeman, and A. E. Rogers, "Medical hyperspectral imaging to facilitate residual tumor identification during surgery," *Cancer Biology & Therapy*, vol. 6, pp. 439–446, Mar. 2007.

[23] H. Akbari, L. Halig, D. M. Schuster, B. Fei, A. Osunkoya, V. Master, P. Nieh, and G. Chen, "Hyperspectral imaging and quantitative analysis for prostate cancer detection," *Journal of Biomedical Optics*, vol. 17, p. 076005, July 2012.

[24] R. L. Greenman, S. Panasyuk, X. Wang, T. E. Lyons, T. Dinh, L. Longoria, J. M. Giurini, J. Freeman, L. Khaodhiar, and A. Veves, "Early changes in the skin microcirculation and muscle metabolism of the diabetic foot," *The Lancet*, vol. 366, pp. 1711–1717, Nov. 2005.

[25] B. S. Sorg, B. J. Moeller, O. Donovan, Y. Cao, and M. W. Dewhirst, "Hyperspectral imaging of hemoglobin saturation in tumor microvasculature and tumor hypoxia development," *Journal of Biomedical Optics*, vol. 10, p. 044004, July 2005.

[26] S. G. Kong, M. E. Martin, and T. VoDinh, "Hyperspectral Fluorescence Imaging for Mouse Skin Tumor Detection," *ETRI Journal*, vol. 28, no. 6, pp. 770–776, 2006.

[27] L. Cancio, A. Batchinsky, J. Mansfield, S. Panasyuk, K. Hetz, D. Martini, B. Jordan, B. Tracey, and J. Freeman, "Hyperspectral Imaging: A New Approach to the Diagnosis of Hemorrhagic Shock," *The Journal of Trauma: Injury, Infection, and Critical Care*, vol. 60, pp. 1087–1095, May 2006.

[28] K. J. Zuzak, S. C. Naik, G. Alexandrakis, D. Hawkins, K. Behbehani, and E. H. Livingston, "Characterization of a Near-Infrared Laparoscopic Hyperspectral Imaging System for Minimally Invasive Surgery," *Analytical Chemistry*, vol. 79, pp. 4709–4715, June 2007.

[29] P. Constantinou, T. Nicklee, D. W. Hedley, S. Damaskinos, and B. C. Wilson, "A high-resolution MACROscope with differential phase contrast, transmitted light, confocal fluorescence, and hyperspectral capabilities for large-area tissue imaging," *IEEE Journal of Selected Topics in Quantum Electronics*, vol. 11, pp. 766–777, July 2005.

[30] S. A. Shah, N. Bachrach, S. J. Spear, D. S. Letbetter, R. A. Stone, R. Dhir, J. W. Prichard, H. G. Brown, and W. A. LaFramboise, "Cutaneous wound analysis using hyperspectral imaging," *BioTechniques*, vol. 34, pp. 408–413, Feb. 2003.

[31] D. T. Dicker, J. Lerner, P. Van Belle, S. F. Barth, D. Guerry, M. Herlyn, D. E. Elder, and W. S. El-Deiry, "Differentiation of normal skin and melanoma using high resolution hyperspectral imaging," *Cancer Biology & Therapy*, vol. 5, pp. 1033–1038, Aug. 2006.

[32] H. Akbari, Y. Kosugi, K. Kojima, and N. Tanaka, "Detection and Analysis of the Intestinal Ischemia Using Visible and Invisible Hyperspectral Imaging," *IEEE Transactions on Biomedical Engineering*, vol. 57, pp. 2011–2017, Aug. 2010.

[33] H. Akbari, K. Uto, Y. Kosugi, K. Kojima, and N. Tanaka, "Cancer detection using infrared hyperspectral imaging," *Cancer Science*, vol. 102, pp. 852–857, Apr. 2011.

[34] M. B. Sinclair, J. A. Timlin, D. M. Haaland, and M. Werner-Washburne, "Design, construction, characterization, and application of a hyperspectral microarray scanner," *Applied Optics*, vol. 43, pp. 2079–2088, Apr. 2004.

[35] V. L. Sutherland, J. A. Timlin, L. T. Nieman, J. F. Guzowski, M. K. Chawla, P. F. Worley, B. Roysam, B. L. McNaughton, M. B. Sinclair, and C. A. Barnes,

"Advanced imaging of multiple mRNAs in brain tissue using a custom hyperspectral imager and multivariate curve resolution," *Journal of Neuroscience Methods*, vol. 160, pp. 144–148, Feb. 2007.

[36] H. Xu, J. Peng, H.-W. Tang, Y. Li, Q.-S. Wu, Z.-L. Zhang, G. Zhou, C. Chen, and Y. Li, "Hadamard transform spectral microscopy for single cell imaging using organic and quantum dot fluorescent probes," *Analyst*, vol. 134, pp. 504–511, Feb. 2009.

[37] R. T. Kester, N. Bedard, L. S. Gao, and T. S. Tkaczyk, "Real-time snapshot hyperspectral imaging endoscope," *Journal of Biomedical Optics*, vol. 16, p. 056005, May 2011.

[38] A. H. Kashani, E. Kirkman, G. Martin, and M. S. Humayun, "Hyperspectral Computed Tomographic Imaging Spectroscopy of Vascular Oxygen Gradients in the Rabbit Retina In Vivo," *PLOS ONE*, vol. 6, p. e24482, Sept. 2011.

[39] E. Clementi, G. C. Brown, N. Foxwell, and S. Moncada, "On the mechanism by which vascular endothelial cells regulate their oxygen consumption," *Proceedings of the National Academy of Sciences of the United States of America*, vol. 96, pp. 1559–1562, Feb. 1999.

[40] R. P. Pandian, V. K. Kutala, N. L. Parinandi, J. L. Zweier, and P. Kuppusamy, "Measurement of oxygen consumption in mouse aortic endothelial cells using a microparticulate oximetry probe," *Archives of Biochemistry and Biophysics*, vol. 420, pp. 169–175, Dec. 2003.

[41] R. N. Pittman, "Oxygen transport in the microcirculation and its regulation," *Microcirculation (New York, N.Y.: 1994)*, vol. 20, pp. 117–137, Feb. 2013.

[42] D. F. Wilson, "Quantifying the role of oxygen pressure in tissue function," *American Journal of Physiology-Heart and Circulatory Physiology*, vol. 294, pp. H11–H13, Jan. 2008.

[43] R. N. Pittman, "Oxygen Gradients in the Microcirculation," *Acta physiologica (Oxford, England)*, vol. 202, pp. 311–322, July 2011.

[44] W. J. Whalen, J. Riley, and P. Nair, "A microelectrode for measuring intracellular PO2.," *Journal of Applied Physiology*, vol. 23, pp. 798–801, Nov. 1967.

[45] N. P. Revsbech, "An oxygen microsensor with a guard cathode," *Limnology and Oceanography*, vol. 34, no. 2, pp. 474–478, 1989.

[46] S. M. Grist, L. Chrostowski, and K. C. Cheung, "Optical Oxygen Sensors for Applications in Microfluidic Cell Culture," *Sensors (Basel, Switzerland)*, vol. 10, pp. 9286–9316, Oct. 2010.

[47] B. A. Wagner, S. Venkataraman, and G. R. Buettner, "The Rate of Oxygen Utilization by Cells," *Free radical biology & medicine*, vol. 51, pp. 700–712, Aug. 2011.

[48] D. G. Buerk, "Measuring Tissue PO2 with Microelectrodes," in *Methods in Enzymology*, vol. 381 of *Oxygen Sensing*, pp. 665–690, Academic Press, Jan. 2004.

[49] I. P. Torres Filho and M. Intaglietta, "Microvessel PO2 measurements by phosphorescence decay method," *The American Journal of Physiology*, vol. 265, pp. H1434–1438, Oct. 1993.

[50] P. Cabrales, A. G. Tsai, and M. Intaglietta, "Modulation of Perfusion and Oxygenation by Red Blood Cell Oxygen Affinity during Acute Anemia," *American Journal of Respiratory Cell and Molecular Biology*, vol. 38, pp. 354–361, Mar. 2008.

[51] P. Cabrales, A. G. Tsai, and M. Intaglietta, "BALANCE BETWEEN VASOCONSTRICTION AND ENHANCED OXYGEN DELIVERY," *Transfusion*, vol. 48, pp. 2087–2095, Oct. 2008.

[52] A. G. Tsai, P. Cabrales, P. C. Johnson, M. Intaglietta, A. S. Golub, and R. N. Pittman, "Effect of oxygen consumption by measuring method on PO2 transients associated with the passage of erythrocytes in capillaries of rat mesentery," *American Journal of Physiology. Heart and Circulatory Physiology*, vol. 289, pp. H1777; author reply H1778–1779, Oct. 2005.

[53] N. J. Nilsson, "Oximetry," *Physiological Reviews*, vol. 40, pp. 1–26, Jan. 1960.

[54] A. Jubran, "Pulse oximetry," *Critical Care*, vol. 19, no. 1, 2015.

[55] A. Seiyama, S. S. Chen, T. Imai, H. Kosaka, and T. Shiga, "Assessment of rate of O2 release from single hepatic sinusoids of rats," *American Journal of Physiology-Heart and Circulatory Physiology*, vol. 267, pp. H944–H951, Sept. 1994.

[56] R. N. Pittman, "In vivo photometric analysis of hemoglobin," *Annals of Biomedical Engineering*, vol. 14, pp. 119–137, Mar. 1986.

[57] L. Giannoni, F. Lange, and I. Tachtsidis, "Hyperspectral imaging solutions for brain tissue metabolic and hemodynamic monitoring: past, current and future developments," *Journal of Optics*, vol. 20, no. 4, p. 044009, 2018.

[58] D. Malonek and A. Grinvald, "Interactions Between Electrical Activity and Cortical Microcirculation Revealed by Imaging Spectroscopy: Implications for Functional Brain Mapping," *Science*, vol. 272, pp. 551–554, Apr. 1996.

[59] M. Wankhede, N. Agarwal, R. A. Fraga-Silva, C. deDeugd, M. K. Raizada, S. P. Oh, and B. S. Sorg, "Spectral imaging reveals microvessel physiology and function from anastomoses to thromboses," *Journal of Biomedical Optics*, vol. 15, no. 1, p. 011111, 2010.

[60] G. Hanna, A. Fontanella, G. Palmer, S. Shan, D. R. Radiloff, Y. Zhao, D. Irwin, K. Hamilton, A. Boico, C. A. Piantadosi, G. Blueschke, M. Dewhirst, T. McMahon, and T. Schroeder, "Automated measurement of blood flow velocity and direction and hemoglobin oxygen saturation in the rat lung using intravital microscopy," *American Journal of Physiology-Lung Cellular and Molecular Physiology*, vol. 304, pp. L86–L91, Nov. 2012.

[61] S.-w. Choe, A. P. Acharya, B. G. Keselowsky, and B. S. Sorg, "Intravital microscopy imaging of macrophage localization to immunogenic particles and co-localized tissue oxygen saturation," *Acta Biomaterialia*, vol. 6, pp. 3491–3498, Sept. 2010.

[62] J. Zhong, N. Rajaram, D. M. Brizel, A. E. Frees, N. Ramanujam, I. Batinic-Haberle, and M. W. Dewhirst, "Radiation induces aerobic glycolysis through reactive oxygen species," *Radiotherapy and Oncology*, vol. 106, pp. 390–396, Mar. 2013.

[63] H. C. Hendargo, Y. Zhao, T. Allenby, and G. M. Palmer, "Snap-shot multispectral imaging of vascular dynamics in a mouse window chamber model," *Optics letters*, vol. 40, pp. 3292–3295, July 2015.

[64] B. Styp-Rekowska, N. M. Disassa, B. Reglin, L. Ulm, H. Kuppe, T. W. Secomb, and A. R. Pries, "An Imaging Spectroscopy Approach for Measurement of Oxygen Saturation and Hematocrit During Intravital Microscopy," *Microcirculation*, vol. 14, pp. 207–221, Jan. 2007.

[65] R. Rasul, M. Harper, and N. Rajaram, "Intravital imaging of tumor bioenergetics in metastatic and non-metastatic breast cancer," in *Diagnosis and*

Treatment of Diseases in the Breast and Reproductive System IV, vol. 10472, p. 104720E, International Society for Optics and Photonics, Feb. 2018.

[66] N. Agarwal, "DYNAMIC SPATIAL AND TEMPORAL CHANGES IN TUMOR MICROVESSEL HEMOGLOBIN SATURATION MEASURED WITH HYPERSPECTRAL IMAGING," p. 71.

[67] M. C. Skala, A. Fontanella, H. Hendargo, M. W. Dewhirst, and J. A. Izatt, "Combined Hyperspectral and Spectral Domain Optical Coherence Tomography Microscope for Non-invasive Hemodynamic Imaging," *Optics letters*, vol. 34, pp. 289–291, Feb. 2009.

[68] J. A. Lee, R. T. Kozikowski, and B. S. Sorg, "Combination of spectral and fluorescence imaging microscopy for wide-field in vivo analysis of microvessel blood supply and oxygenation," *Optics Letters*, vol. 38, pp. 332–334, Feb. 2013.

[69] B. S. Sorg, M. E. Hardee, N. Agarwal, B. J. Moeller, and M. W. Dewhirst, "Spectral imaging facilitates visualization and measurements of unstable and abnormal microvascular oxygen transport in tumors," *Journal of Biomedical Optics*, vol. 13, p. 014026, Jan. 2008.

[70] G. M. Palmer, A. N. Fontanella, G. Zhang, G. Hanna, C. L. Fraser, and M. W. Dewhirst, "Optical imaging of tumor hypoxia dynamics," *Journal of Biomedical Optics*, vol. 15, p. 066021, Nov. 2010.

[71] A. N. Fontanella, T. Schroeder, D. W. Hochman, R. E. Chen, G. Hanna, M. M. Haglund, T. W. Secomb, G. M. Palmer, and M. W. Dewhirst, "Quantitative Mapping of Hemodynamics in the Lung, Brain, and Dorsal Window Chamber-Grown Tumors Using a Novel, Automated Algorithm," *Microcirculation*, vol. 20, no. 8, pp. 724–735, 2013.

[72] D. R. McCormack, A. J. Walsh, W. Sit, C. L. Arteaga, J. Chen, R. S. Cook, and M. C. Skala, "In vivo hyperspectral imaging of microvessel response to trastuzumab treatment in breast cancer xenografts," *Biomedical Optics Express*, vol. 5, pp. 2247–2261, June 2014.

[73] C. Han, S.-W. Choe, Y. H. Kim, A. P. Acharya, B. G. Keselowsky, B. S. Sorg, Y.-J. Lee, and S. P. Oh, "VEGF neutralization can prevent and normalize arteriovenous malformations in an animal model for hereditary hemorrhagic telangiectasia 2," *Angiogenesis*, vol. 17, pp. 823–830, Oct. 2014.

[74] S. Tual-Chalot, P. Oh, and H. M. Arthur, "Mouse Models of Hereditary Haemorrhagic Telangiectasia: Recent Advances and Future Challenges," *Frontiers in Genetics*, vol. 6, 2015.

[75] B. Khoobehi, J. M. Beach, and H. Kawano, "Hyperspectral Imaging for Measurement of Oxygen Saturation in the Optic Nerve Head," *Investigative Ophthalmology & Visual Science*, vol. 45, pp. 1464–1472, May 2004.

[76] A. G. Tsai, P. Cabrales, R. M. Winslow, and M. Intaglietta, "Microvascular oxygen distribution in awake hamster window chamber model during hyperoxia," *American Journal of Physiology-Heart and Circulatory Physiology*, vol. 285, pp. H1537–H1545, Oct. 2003.

[77] C. Vaiphasa, "Consideration of smoothing techniques for hyperspectral remote sensing," *ISPRS Journal of Photogrammetry and Remote Sensing*, vol. 60, pp. 91–99, Apr. 2006.

[78] R. Koprowski, S. J. Teper, B. Wglarz, E. Wylgaa, M. Krejca, and Z. Wrbel, "Fully automatic algorithm for the analysis of vessels in the angiographic image of the eye fundus," *BioMedical Engineering OnLine*, vol. 11, p. 35, June 2012.

[79] F. C. Wireko and D. J. Abraham, "The crystal state binding of dithionite to deoxy-hemoglobin," *Protein Engineering*, vol. 5, pp. 3–5, Jan. 1992.

[80] J. Canny, "A Computational Approach to Edge Detection," in *Readings in Computer Vision* (M. A. Fischler and O. Firschein, eds.), pp. 184–203, San Francisco (CA): Morgan Kaufmann, Jan. 1987.

[81] M. Ester, H.-P. Kriegel, J. Sander, and X. Xu, "A density-based algorithm for discovering clusters in large spatial databases with noise," pp. 226–231, AAAI Press, 1996.

[82] A. G. Tsai, B. Friesenecker, M. C. Mazzoni, H. Kerger, D. G. Buerk, P. C. Johnson, and M. Intaglietta, "Microvascular and tissue oxygen gradients in the rat mesentery," *Proceedings of the National Academy of Sciences of the United States of America*, vol. 95, pp. 6590–6595, June 1998.

[83] P. Cabrales, P. Nacharaju, B. N. Manjula, A. G. Tsai, S. A. Acharya, and M. Intaglietta, "Early difference in tissue pH and microvascular hemodynamics in hemorrhagic shock resuscitation using polyethylene glycol-albumin- and hydroxyethyl starch-based plasma expanders," *Shock (Augusta, Ga.)*, vol. 24, pp. 66–73, July 2005.

[84] O. Yalcin and P. Cabrales, "Increased hemoglobin O2 affinity protects during acute hypoxia," *American Journal of Physiology - Heart and Circulatory Physiology*, vol. 303, pp. H271–H281, Aug. 2012.

[85] B. Grassi, L. B. Gladden, C. M. Stary, P. D. Wagner, and M. C. Hogan, "Peripheral O2 diffusion does not affect Vo 2 on-kinetics in isolated in situ canine muscle," *Journal of Applied Physiology*, vol. 85, pp. 1404–1412, Oct. 1998.

[86] H. F. Bunn and R. O. Poyton, "Oxygen sensing and molecular adaptation to hypoxia," *Physiological Reviews*, vol. 76, pp. 839–885, July 1996.

[87] E. D. Robin, B. J. Murphy, and J. Theodore, "Coordinate regulation of glycolysis by hypoxia in mammalian cells," *Journal of Cellular Physiology*, vol. 118, pp. 287–290, Mar. 1984.

[88] K. L. Eales, K. E. R. Hollinshead, and D. A. Tennant, "Hypoxia and metabolic adaptation of cancer cells," *Oncogenesis*, vol. 5, p. e190, Jan. 2016.

[89] N. S. Chandel, D. S. McClintock, C. E. Feliciano, T. M. Wood, J. A. Melendez, A. M. Rodriguez, and P. T. Schumacker, "Reactive Oxygen Species Generated at Mitochondrial Complex III Stabilize Hypoxia-inducible Factor-1 during Hypoxia A MECHANISM OF O2 SENSING," *Journal of Biological Chemistry*, vol. 275, pp. 25130–25138, Aug. 2000.

[90] G. L. Wang and G. L. Semenza, "Oxygen sensing and response to hypoxia by mammalian cells," *Redox Report*, vol. 2, pp. 89–96, Apr. 1996.

[91] E. Paternotte, C. Gaucher, P. Labrude, J.-F. Stoltz, and P. Menu, "Review: behaviour of endothelial cells faced with hypoxia," *Bio-Medical Materials and Engineering*, vol. 18, no. 4-5, pp. 295–299, 2008.

[92] P. C. Johnson, K. Vandegriff, A. G. Tsai, and M. Intaglietta, "Effect of acute hypoxia on microcirculatory and tissue oxygen levels in rat cremaster muscle," *Journal of Applied Physiology*, vol. 98, pp. 1177–1184, Apr. 2005.

[93] E. A. Burykh, S. V. Nesterov, S. I. Soroko, and N. Y. Volkov, "Relationships between Cerebral Blood Flow Dynamics and Bioelectric Activity of the Human Brain in Experimental Acute Hypoxia," *Human Physiology*, vol. 28, pp. 657–663, Nov. 2002.

[94] C. Tachibana, T. Fukada, R. Hasegawa, K. Satoh, Y. Furuya, and Y. Ohe, "[Accuracy of a pulse oximeter during hypoxia]," *Masui. The Japanese Journal of Anesthesiology*, vol. 45, pp. 479–482, Apr. 1996.

[95] A. Louie, J. R. Feiner, P. E. Bickler, L. Rhodes, M. Bernstein, and J. Lucero, "Four Types of Pulse Oximeters Accurately Detect Hypoxia during Low Perfusion and Motion," *Anesthesiology*, vol. 128, pp. 520–530, Mar. 2018.

[96] S. E. LeBlanc and D. R. Coughanowr, *Process systems analysis and control*. McGraw-Hill chemical engineering series, Boston: McGraw-Hill Higher Education, 3rd ed ed., 2009. OCLC: ocn226308145.

[97] M. J. Poulin, P. J. Liang, and P. A. Robbins, "Dynamics of the cerebral blood flow response to step changes in end-tidal PCO2 and PO2 in humans," *Journal of Applied Physiology*, vol. 81, pp. 1084–1095, Sept. 1996.

[98] H. Bicher, D. Reneau, D. Bruley, and M. Knisely, "Brain oxygen supply and neuronal activity under normal and hypoglycemic conditions," *American Journal of Physiology-Legacy Content*, vol. 224, pp. 275–282, Feb. 1973.

[99] S. J. Schiff and G. G. Somjen, "Overshoot of oxygen pressure in post-hypoxic brain tissue: a re-evaluation," *Brain Research*, vol. 344, pp. 150–153, Sept. 1985.

[100] R. Hashimoto, T. Kurata, M. Sekine, K. Nakano, T. Ohnishi, and H. Haneishi, "Two-wavelength oximetry of tissue microcirculation based on sidestream dark-field imaging," *Journal of Biomedical Optics*, vol. 24, p. 031013, Oct. 2018.

[101] F. F. M. d. Mul, F. Morales, A. J. Smit, and R. Graaff, "A model for post-occlusive reactive hyperemia as measured with laser-Doppler perfusion monitoring," *IEEE Transactions on Biomedical Engineering*, vol. 52, pp. 184–190, Feb. 2005.

[102] J. K. Gourley and D. D. Heistad, "Characteristics of reactive hyperemia in the cerebral circulation," *American Journal of Physiology-Heart and Circulatory Physiology*, vol. 246, pp. H52–H58, Jan. 1984.

[103] R. Rosenberry, M. Munson, S. Chung, T. J. Samuel, J. Patik, W. J. Tucker, M. J. Haykowsky, and M. D. Nelson, "Age-related microvascular dysfunction: novel insight from near-infrared spectroscopy," *Experimental Physiology*, vol. 103, no. 2, pp. 190–200, 2018.

[104] K. Kvernebo, C. E. Slasgsvold, and E. Stranden, "Laser Doppler flowmetry in evaluation of skin post-ischaemic reactive hyperaemia. A study in healthy volunteers and atherosclerotic patients," *The Journal of Cardiovascular Surgery*, vol. 30, pp. 70–75, Feb. 1989.

[105] R. del Guercio, G. Leonardo, and M. R. Arpaia, "Evaluation of postischemic hyperemia on the skin using laser Doppler velocimetry: study on patients with claudicatio intermittens," *Microvascular Research*, vol. 32, pp. 289–299, Nov. 1986.

[106] S. Lacroix, M. Gayda, V. Gremeaux, M. Juneau, J.-C. Tardif, and A. Nigam, "Reproducibility of near-infrared spectroscopy parameters measured during brachial artery occlusion and reactive hyperemia in healthy men," *Journal of Biomedical Optics*, vol. 17, p. 077010, July 2012.

[107] C. P. Favazza, L. V. Wang, and L. A. Cornelius, "<!– *** Custom HTML *** –>*In vivo* functional photoacoustic microscopy of cutaneous microvasculature in human skin," *Journal of Biomedical Optics*, vol. 16, p. 026004, Feb. 2011.

[108] J. L. Jasperse, J. K. Shoemaker, E. J. Gray, and P. S. Clifford, "Positional differences in reactive hyperemia provide insight into initial phase of exercise hyperemia," *Journal of Applied Physiology*, vol. 119, pp. 569–575, Sept. 2015.

[109] J. H. Lombard and B. R. Duling, "Multiple mechanisms of reactive hyperemia in arterioles of the hamster cheek pouch," *American Journal of Physiology-Heart and Circulatory Physiology*, vol. 241, pp. H748–H755, Nov. 1981.

[110] B. Treml, A. Kleinsasser, K.-H. Stadlbauer, I. Steiner, W. Pajk, M. Pilch, M. Burtscher, and H. Knotzer, "Cutaneous Microvascular Blood Flow and Reactivity in Hypoxia," *Frontiers in Physiology*, vol. 9, Mar. 2018.

[111] A. Paparde, L. Plakane, K. Circenis, and J. I. Aivars, "Effect of acute systemic hypoxia on human cutaneous microcirculation and endothelial, sympathetic and myogenic activity," *Microvascular Research*, vol. 102, pp. 1–5, Nov. 2015.

[112] A. G. Hudetz, B. B. Biswal, G. Fehr, and J. P. Kampine, "Effects of Hypoxia and Hypercapnia on Capillary Flow Velocity in the Rat Cerebral Cortex," *Microvascular Research*, vol. 54, pp. 35–42, July 1997.

[113] A. D. Harris, K. Murphy, C. M. Diaz, N. Saxena, J. E. Hall, T. T. Liu, and R. G. Wise, "Cerebral blood flow response to acute hypoxic hypoxia," *Nmr in Biomedicine*, vol. 26, pp. 1844–1852, Dec. 2013.

[114] D. Bereczki, L. Wei, T. Otsuka, V. Acuff, K. Pettigrew, C. Patlak, and J. Fenstermacher, "Hypoxia Increases Velocity of Blood Flow through Parenchymal Microvascular Systems in Rat Brain," *Journal of Cerebral Blood Flow & Metabolism*, vol. 13, pp. 475–486, May 1993.

[115] K. Heerlein, A. Schulze, L. Hotz, P. Brtsch, and H. Mairburl, "Hypoxia Decreases Cellular ATP Demand and Inhibits Mitochondrial Respiration of A549 Cells," *American Journal of Respiratory Cell and Molecular Biology*, vol. 32, pp. 44–51, Jan. 2005.

[116] I. Papandreou, R. A. Cairns, L. Fontana, A. L. Lim, and N. C. Denko, "HIF-1 mediates adaptation to hypoxia by actively downregulating mitochondrial oxygen consumption," *Cell Metabolism*, vol. 3, pp. 187–197, Mar. 2006.

[117] D. C. Fuhrmann and B. Brne, "Mitochondrial composition and function under the control of hypoxia," *Redox Biology*, vol. 12, pp. 208–215, Feb. 2017.

[118] P. Hernansanz-Agustn, A. Izquierdo-lvarez, F. J. Snchez-Gmez, E. Ramos, T. Villa-Pia, S. Lamas, A. Bogdanova, and A. Martnez-Ruiz, "Acute hypoxia produces a superoxide burst in cells," *Free Radical Biology and Medicine*, vol. 71, pp. 146–156, June 2014.

[119] J. W. Cannon, "Hemorrhagic Shock," *New England Journal of Medicine*, vol. 378, pp. 370–379, Jan. 2018.

[120] M. Halmin, F. Chiesa, S. K. Vasan, A. Wikman, R. Norda, K. Rostgaard, O. B. Vesterager Pedersen, C. Erikstrup, K. R. Nielsen, K. Titlestad, H. Ullum, H. Hjalgrim, and G. Edgren, "Epidemiology of Massive Transfusion: A Binational Study From Sweden and Denmark*," Mar. 2016.

[121] N. T. Veith, T. Histing, M. D. Menger, T. Pohlemann, and T. Tschernig, "Helping prometheus: liver protection in acute hemorrhagic shock," *Annals of Translational Medicine*, vol. 5, May 2017.

[122] L. Yu, A. C. Seguro, and A. S. Rocha, "Acute renal failure following hemorrhagic shock: protective and aggravating factors," *Renal Failure*, vol. 14, no. 1, pp. 49–55, 1992.

[123] A. M. Master, S. Dack, H. Horn, B. I. Freedman, and L. E. Field, "Acute Coronary Insufficiency Due to Acute Hemorrhage: An Analysis of One Hundred and Three Cases," *Circulation*, vol. 1, pp. 1302–1317, June 1950.

[124] S. A. Tisherman, "Trauma fluid resuscitation in 2010," *The Journal of Trauma*, vol. 54, pp. S231–234, May 2003.

[125] R. N. Bilkovski, E. P. Rivers, and H. M. Horst, "Targeted resuscitation strategies after injury," *Current Opinion in Critical Care*, vol. 10, pp. 529–538, Dec. 2004.

[126] C. Messmer, O. Yalcin, A. F. Palmer, and P. Cabrales, "SMALL VOLUME RESUSCITATION FROM HEMORRHAGIC SHOCK WITH POLYMERIZED HUMAN SERUM ALBUMIN," *The American journal of emergency medicine*, vol. 30, pp. 1336–1346, Oct. 2012.

[127] D. Ortiz, M. Barros, S. Yan, and P. Cabrales, "Resuscitation from hemorrhagic shock using polymerized hemoglobin compared to blood," *The American journal of emergency medicine*, vol. 32, pp. 248–255, Mar. 2014.

[128] R. Wettstein, A. G. Tsai, D. Erni, R. M. Winslow, and M. Intaglietta, "Resuscitation with polyethylene glycol-modified human hemoglobin improves microcirculatory blood flow and tissue oxygenation after hemorrhagic shock in awake hamsters," *Critical Care Medicine*, vol. 31, pp. 1824–1830, June 2003.

[129] M. Legrand, E. G. Mik, G. M. Balestra, R. Lutter, R. Pirracchio, D. Payen, and C. Ince, "Fluid Resuscitation Does Not Improve Renal Oxygenation during Hemorrhagic Shock in Rats," *Anesthesiology: The Journal of the American Society of Anesthesiologists*, vol. 112, pp. 119–127, Jan. 2010.

[130] R. W. Barbee, P. S. Reynolds, and K. R. Ward, "Assessing shock resuscitation strategies by oxygen debt repayment," *Shock (Augusta, Ga.)*, vol. 33, pp. 113–122, Feb. 2010.